Draft version May 25, 2018
Typeset using LaTeX **twocolumn** style in AASTeX62

Do Lyα absorbers co-rotate with galaxies?

David M. French, Bart P. Wakker[1]

[1] *Department of Astronomy, University of Wisconsin, Madison, WI 53706, USA*

ABSTRACT

We present results of a study comparing the relative velocity of Lyα absorbers to the rotation direction and velocity of nearby galaxy disks in the nearby Universe ($z \leq 0.03$). We have obtained rotation curves via long-slit spectra of 12 galaxies with the Southern African Large Telescope, and combine this dataset with an additional XXXX galaxies with published rotation curves from the literature. Each galaxy appears within $3R_{\rm vir}$ of a QSO with available COS data covering the relevant Lyα wavelength range. We find...

Keywords: galaxies:intergalactic medium, galaxies:evolution, galaxies:halos, quasars: absorption lines

1. INTRODUCTION

Our current ΛCDM cosmology picture describes galaxies forming hierarchically out of overdensities in the underlying dark matter distribution. As the surrounding intergalactic medium (IGM) is funneled toward a growing galaxy, simulations predict the angular momentum of the inflowing gas is redistributed onto the disk and seeds the overall rotation of the galaxy (e.g., Stewart et al. (2011a); Chen et al. (2003); Sharma & Steinmetz (2005); Brook et al. (2011); Kimm et al. (2011); Pichon et al. (2011); Stewart et al. (2013)). As this infalling gas is responsible for birthing and continuing to feed the galaxies throughout their lifetimes, it is expected that the extended gaseous halos should rotate in the same sense as both the galactic disks and dark matter halos.

In this ΛCDM picture, the accretion falls broadly into two types. In the so-called "hot-mode", when gas encounters the galaxy halo it shock-heats at the virial radius. The inner, more dense region of this hot gaseous halo then rains down onto the disk as it radiatively cools (Fillmore & Goldreich 1984; Bertschinger 1985, Danovich et al. (2012), Shen et al. (2013)). However, most gas arrives cold ($T \sim 10^4$ K) from the IGM, and the proposed radiative shock is unstable to cooling. Thus this hot-halo scenario may not actually be created (Birnboim & Dekel 2003; Keres et al. 2005; Ocvirk, Pichon & Teyssier 2008; Brooks et al. 2009; Dekel et al. 2009).

In the alternative mode, "cold-mode" accretion, filaments of gas from the IGM should merge smoothly with the disk, thus converting a significant fraction of their infall velocity to rotational velocity of the galaxy. (Keres et al. 2005, Stewart et al. (2017)). Powell, Slyz & Devriendt (2011) spectacularly confirmed these conjectures by showing that indeed, the accreting filaments connect rather smoothly to the disc. This cold-mode of accretion likely dominates the global growth of all but the most massive halos at high redshifts ($z \gtrsim 3$), and the growth of lower mass ($M_{\rm halo} \leq 5 \times 10^{11}\ M_*$) objects at late times (Dekel & Birnboim 2006). Furthermore, cosmological SPH simulations such as those by Stewart et al. (2011b, 2013) **NEED MORE CURRENT ONES TOO** suggests that halo gas should co-rotate with disk-gas out to at least 100 kpc, and that absorption in intervening QSO sightlines should be able to accurately capture this rotation signature.

Some observational evidence of cold-mode accretion has been obtained at higher redshifts (Kaczprak?, Steidel?). In pioneering studies focusing on the Mg II absorber kinematics and their connection with neighboring galaxies, Charlton & Churchill (1998) Steidel et al. (2002), and later (**Kaczprak?? and more?**) find tantalizing evidence that a significant fraction of Mg II absorbers have velocities that can be explained by an extended gaseous disk. Additionally, Diamond-Stanic et al. (2016) detect co-rotating Hα emission and Mg II and Fe II absorption toward a Milky Way-like galaxy at $z = 0.413$. However, as noted by Steidel 2002, a rotating *halo* may be a better model than a simple extended thick disk model.

However, the picture may have changed since $z \sim 0.5$, the epoch most of these Mg II are probing. By $z \sim 0$ simulations (e.g., ...) predict a drop-off in cold-mode accretion and a decrease in the density of IGM filaments. Observational confirmation has been even more inconclusive in this low-redshift regime. In the largest such study, involving Lyα absorber-galaxy kinematics, Côté et al. (2005) probed the halos of nine galaxies using *HST* observed background QSOs, and found that large warps would be needed to explain the velocity of H I absorbers by an extended rotating disk. Wakker & Savage (2009) compiled a sample of 4 galaxy-QSO systems from the literature, finding only 1/4 of Lyα absorbers appeared to co-rotate with the associated galaxy disk. Approaching the question from a different angle, Bowen et al. (2016) probed the halo of a single galaxy, NGC1097, with 4 nearby QSO sightlines, and suggests that an extended, slowly rotating disk with additional inflowing IGM material best matches observations.

To make progress here, we have obtained rotation curves for 12 nearby spiral galaxies which are located within $3R_{vir}$ kpc of a background QSO observed by the Cosmic Origins Spectrograph (COS) on *HST*. A literature search yielded an additional 16 galaxies with published rotation curves and known orientations. Each of these is probed by at least one QSO within $3R_{vir}$.

In Section 2 we describe the selection and reduction of both SALT and COS spectra. In Section 3 we present a new rotating halo model we have developed to aid in the interpretation of our observations. We then discuss each galaxy-QSO system in detail in Section B. In Section 4 we discuss the overall results of this exercise and present a physically-motivated interpretation of these results. See Section 5 for a summary of our results and conclusions.

2. DATA AND ANALYSIS

2.1. *SALT Data*

Our sample contains 12 galaxies observed with the Southern African Large Telescope (SALT) Robert Stobie Spectrograph (RSS) in longslit mode. These 12 were selected from a larger pool of 48 submitted targets by the SALT observing queue. These 48 possible targets were chosen for their proximity to background QSOs whose spectra contained promising Lyα lines. Finally, we only included galaxies with $z \leq 0.33$ ($cz \leq 10,000$ km s^{-1}), angular sizes less than 6' to enable easy sky subtraction without taking additional exposures, and surface brightnesses sufficient to keep exposure times below $\sim 1300s$. Table 1 summarizes these observations. Data was taken for 2 additional galaxies, NGC3640 and NGC2962, but proved unusable due to issues with spectral identification and low signal-to-noise (respectively).

All SALT galaxy spectra were reduced and extracted using the standard PySALT reduction package (**CITATION**), which includes procedures to prepare the data, correct for gain, cross-talk, bias, and overscan, and finally mosaic the images from the 3 CCDs. Next, we rectify the images with wavelength solutions found via Ne and Ar arc lamp spectra line identification. Finally, we perform a basic sky subtraction using an off-sky portion of the spectrum, and extract 5-10 pixel wide 1-D strips from the reduced 2-D spectrum.

For each 1-D spectrum, we identify the Hα emission lines and perform a non-linear least-squares Voigt profile fit using the Python package LMFIT[1]. The line centroid and 1σ standard errors are returned, and these fits are then shifted to rest-velocity based on the galaxy systemic redshift and heliocentric velocity corrections are calculated with the IRAF rvcorrect procedure. The final rotation velocity is calculated by then applying the inclination correction, $v_{rot} = v/\sin(i)$. Final errors are calculated as a quadrature sum of 1σ fit errors, systemic redshift error, and inclination uncertainty as follows:

$$\sigma^2 = \left(\frac{\partial v_{rot}}{\partial \lambda_{obs}}\right)^2 (\Delta\lambda_{obs})^2 + \left(\frac{\partial v_{rot}}{\partial v_{sys}}\right)^2 (\Delta v_{sys})^2 + \left(\frac{\partial v_{rot}}{\partial i}\right)^2 (\Delta i)^2, \tag{1}$$

where $\Delta\lambda_{obs}$, Δv_{sys}, and Δi are the errors in observed line center, galaxy redshift, and inclination, respectively.

We determine the inclination error by calculating the standard deviation of the set of all axis ratio values available in NED for each galaxy. The final physical scale is calculated using the SALT image scale of 0.1267 arcsec/pixel, multiplied by the 4-pixel spatial binning, and converted to physical units using a redshift-independent distance if available, and a Hubble flow estimate if not. We adopt a Hubble constant of $H_0 = 71$ km s^{-1} Mpc^{-1} throughout.

Finally, we calculate our approaching and receding velocities via a weighted mean of the outer 1/2 of each rotation curve, with errors calculated as weighted standard errors in the mean. Our final redshifts are calculated by forcing symmetric rotation, such that the outer 1/2 average velocity for each side matches in magnitude. See Appendix **??** for rotation curves and slit-position charts for each observed galaxy.

2.2. *COS Spectra*

The Barbara A. Mikulski Archive for Space Telescopes (MAST) archives yield 19 QSO targets observed by COS which lie within 500 kpc of our SALT galaxies. These targets vary widely in signal-to-noise from approximately 5 to 100 due to our choosing them based only on their proximity to galaxies with known rotation. The reduction procedure for these spectra follow those described by French & Wakker (2017) and Wakker et al. (2015). In short, spectra are processed with CALCOS v3.0 or higher and combined via the method of Wakker et al. (2015), which helps corrects the COS wavelength scale misalignments produced by CALCOS. Multiple exposures are combined via alignment with Galactic 21cm absorption spectra and summing total counts per pixel before converting to flux. The COS instrument is described in detail by Green et al. (2012).

3. HALO ROTATION MODEL

In order to better understand how QSO sightlines probe intervening velocity structure we have developed

[1] http://cars9.uchicago.edu/software/python/lmfit/contents.html

Table 1. SALT Galaxy Observations

Galaxy	R.A.	Dec.	Measured $v_{\rm sys}$ (km s^{-1})	Published $v_{\rm sys}$ (km s^{-1})	Type	Grating	$v_{\rm rot}$ (km s^{-1})	$v_{\rm rot}/\sin(i)$ (km s^{-1})	Obs. Date	$T_{\rm exp}$ (ks)
(12)	(13)	(14)	(15)	(16)	(17)	(18)	(19)	(20)	(21)	(22)
CGCG039-137	11 21 27.0	+03 26 41.7	6918 ± 24	6902 ± 52^a	Scd	PG2300	132 ± 16	139 ± 26	05 11 2016	700
ESO343-G014	21 37 45.2	−38 29 33.2	9139 ± 32	9162 ± 45^b	S	PG2300	203 ± 32	203 ± 32	05 16 2016	1000
IC5325	23 28 43.4	−41 20 00.5	1512 ± 8	1503 ± 7^c	SAB(rs)bc	PG2300	53 ± 5	125 ± 39	05 17 2016	600
MCG-03-58-009	22 53 40.9	−17 28 44.0	9015 ± 19	9030 ± 10^d	Sc	PG2300	150 ± 12	171 ± 23	05 16 2016	1200
NGC1566	04 20 00.4	−54 56 16.1	1502 ± 15	1504 ± 2^e	SAB(rs)bc	PG2300	64 ± 8	195 ± 47	10 18 2016	400
NGC3513	11 03 46.1	−23 14 43.8	1204 ± 12	1194 ± 7^c	SB(s)c	PG2300	11 ± 10	22 ± 24	05 26 2016	600
NGC3633	11 20 26.2	+03 35 08.2	2587 ± 7	2600 ± 2^f	SAa	PG2300	149 ± 6	157 ± 9	05 11 2016	1200
NGC4536	12 34 27.1	+02 11 17.3	1867 ± 33	1808 ± 1^g	SAB(rc)bc	PG2300	129 ± 9	148 ± 41	05 11 2016	1300
NGC4939	13 04 14.4	−10 20 22.6	3093 ± 33	3110 ± 4^e	SA(s)bc	PG2300	204 ± 25	275 ± 66	05 14 2016	500
NGC5364	13 56 12.0	+05 00 52.1	1238 ± 17	1241 ± 4^c	SA(rs)bc pec	PG2300	130 ± 13	155 ± 22	05 11 2016	700
NGC5786	14 58 56.3	−42 00 48.1	2975 ± 22	2998 ± 5^h	SAB(s)bc	PG2300	156 ± 10	172 ± 25	05 11 2016	250
UGC09760	15 12 02.4	+01 41 55.5	2094 ± 16	2023 ± 2^i	Sd	PG2300	46 ± 10	46 ± 16	05 11 2016	500

Note—SALT targeted galaxies. Columns are as follows: 1) the galaxy name, 2), 3) R.A., Dec. in J2000, 4) galaxy systemic velocity, 5) morphological type (RC3), 6) RSS grating used, 7) approaching side velocity, 8) receding side velocity, 9) observation date, and 10) exposure time

References—a. Abazajian et al. (2005); b. Jones et al. (2009); c. Corwin et al. (1994); d. Mathewson & Ford (1996); e. Koribalski et al. (2004); f. Lu et al. (1993); g. Grogin et al. (1998); h. di Nella et al. (1996); i, Giovanelli et al. (1997)

a simple halo gas rotation model. This model is seeded by an observed rotation curve (or whatever rotation curve-esque data suits ones fancy). The input rotation curve is then extrapolated out to a radius of $3R_{\rm vir}$ and height of $2R_{\rm vir}$ to form a coherently rotating halo. For each galaxy-QSO pair we created 2 rotation models: 1) a purely cylindrical halo with constant velocity, and 2) a cylindrical model with rotation velocities which smoothly decline based on a Navarro-Frenk-White (NFW) profile fit (Navarro et al. 1996, 1997) as a function of radius.

For the first, purely cylindrical model, the input rotation curve is interpolated via linear spline and extended out to $3R_{vir}$ based on the average velocity of the outer 1/2 radius. For the second model, we fit an NFW rotation velocity profile to the input rotation curve. The form of this fit is as follows:

$$V(R) = V_{200}\left[\frac{\ln(1+cx) - cx/(1+cx)}{x[\ln(1+c) - c/(1+c)]}\right]^{\frac{1}{2}}, \qquad (2)$$

where $x = R/R_{200}$, with R_{200} being the radius at which the density contrast with respect to the critical density of the universe exceeds 200, $c = R_{200}/R_s$, with R_s being the characteristic radius of the halo, and V_{200} being the characteristic velocity at R_{200}. We have taken this form from de Blok et al. (2008). The resulting NFW fits tend to be somewhat poor toward the inner parts of the rotation curve (as has been noted by others, e.g., Côté et al. (2005)). Regardless, we are most interested in achieving a physically-motivated velocity profile in the outer halo regions, for which these fits are certainly adequate.

Next, we project this interpolated rotation curve onto a plane oriented to a faux QSO sightline identically to the input galaxy-QSO pair orientation. By stacking multiple rotation-planes in the galaxy z-axis direction, we then create a simple cylindrical halo model embedded with the fit and extrapolated rotation curve. Finally, each rotation-plane in the stack is projected onto the faux sightline. The result is a function representing the rotation velocity encountered by the sightline as a function of velocity (i.e., distance) along it. Each model produces the velocity a co-rotating absorber would project onto the spectrum as a function of velocity along the sightline. We then collapse this into a range of possible observed velocities by summing the x- and y-components along the allowed range. This has the affect of combining *both* the projected rotation velocity *and* the physical velocity separation between an absorber and the galaxy (Δv) into a single velocity range, which we then can compare to the measured absorption velocity ($v_{\rm Ly\alpha}$).

Figure 1 illustrates an example rotation curve for our SALT galaxy NGC3633, along with our linear-spline and NFW fits, a 3D halo mockup, and the resulting cylindrical and NFW model output velocity distributions. In most cases, and as seen in this example, the two model outputs have similar *shape*, but the NFW profile fit usually results in a lower velocity range (i.e., closer to systemic). Because we combine projected velocity with velocity along the sightline, many models allow for an absorber to have the wrong sign of Δv. For example, an absorber on the approaching side of a halo but at the distant edge would end up with a range of positive Δv consistent with co-rotation because the relatively posi-

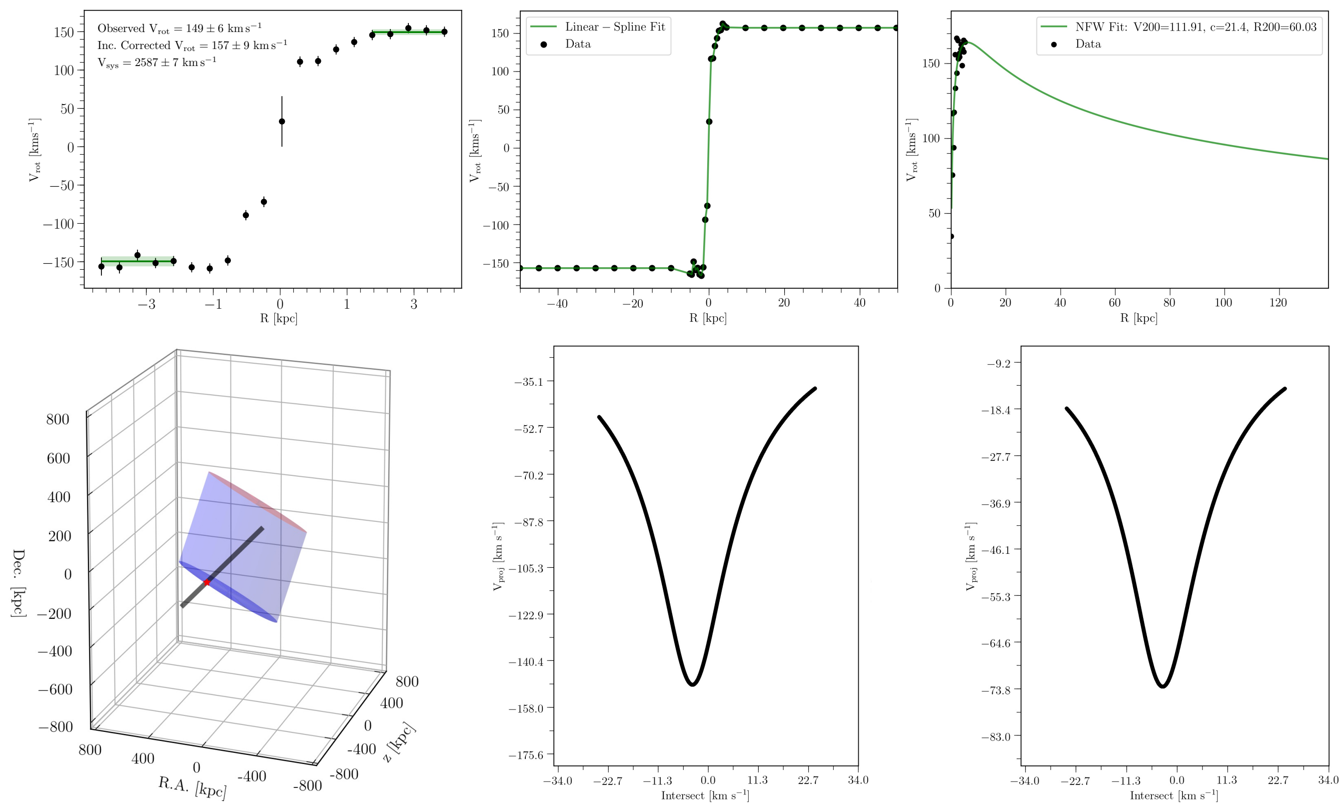

Figure 1. Example rotation curve and model for NGC3633. Top-Left: The rotation curve obtained by SALT-RSS. Data and errors are shown in black, the mean rotation velocity for the outer 1/2 is shown in solid green, and the 1σ error-in-the-mean is shown in shaded green. Top-Middle: The rotation curve is again shown in black, with additional points added to each side based on the outer 1/2 mean velocity. A linear-spline interpolation is overlaid in green. Top-Right: Again the observed rotation curve is shown in black, with an NFW profile fit overlaid in green. Bottom-Left: A 3D example plot of our halo rotation model showing the orientation and extent of the NGC3633 model. The approaching extreme edge of the NGC3633 cylindrical halo is shown by dark-blue oval, with the far edge shown in red. The dark-grey line shows the location of the sightline toward RX_J1121.2+0326 as it penetrates the halo, with a red star marking the first intercept point. Bottom-Middle: The resulting distribution of velocities probed by the RX_J1121.2+0326 sightline in our purely cylindrical model is given by the y-axis ("V_{proj}") as a function of pathlength through the halo ("Intersect"). Bottom-Right: Same, but for our NFW profile fit model.

tive redshift component overcomes the relatively negative rotation component.

Table 3. Halo Model Results and Lyα Absorption Properties

#	Galaxy	Target	ρ	Az.	v_{sys}	v_{rot}	$v_{Ly\alpha}$	$W_{Ly\alpha}$	Cyl. Model	NFW Model
			(kpc)	(Deg.)	(km s^{-1})	(km s^{-1})	(km s^{-1})	(mÅ)	(km s^{-1})	(km s^{-1})
(1)	(2)	(3)	(4)	(5)	(6)	(7)	(8)	(9)	(10)	(11)
1	CGCG039-137	RX_J1121.2+0326	99	71	6918	139	6975	678	6882 - 7055	6881 - 7082
2	ESO343-G014	RBS1768	466	74	9139	205	9308	63	8936 - 9149	9017 - 9170
2	ESO343-G014	RBS1768	466	74	9139	205	9360	306	8936 - 9149	9017 - 9170
2	ESO343-G014	RBS1768	466	74	9139	205	9434	161	8936 - 9149	9017 - 9170
3	IC5325	RBS2000	314	64	1512	-125	1598	35	1471 - 1492	1483 - 1513
4	MCG-03-58-009	MRC2251-178	355	71	9015	171	9029	62	8989 - 9152	8973 - 9098

Table 3 continued

Table 2. Summary of QSO Sample

Target	Galaxy	R.A.	Dec.	z	Program	T_{exp} (ks)
(1)	(2)	(3)	(4)	(5)	(6)	(7)
1H0419-577	NGC1566	04 26 00.7	-57 12 02.0	0.10400	11686	20429
2E1530+1511	NGC5951	15 33 14.3	+15 01 03.0	0.09000	14071	9348
3C232	NGC3067	09 58 20.9	+32 24 02.0	0.5306 0	8596	44662
3C273.0	NGC4536	12 29 06.7	+02 03 09.0	0.15834	12038	4002
CSO295	NGC3432	10 52 05.6	+36 40 40.0	0.60900	14772	1088
CSO1208	NGC3726	11 40 47.9	+46 22 05.0	0.11500	14729	3052
FBQSJ0908+3246	NGC2770	09 08 38.8	+32 46 20.0	0.25989	14240	7430
H1101-232	NGC3513	11 03 37.7	-23 29 31.0	0.18600	12025	13341
HE0429-5343	NGC1566	04 30 40.0	-53 36 56.0	0.04001	12275	2067
HE1228+0131	NGC4536	12 30 50.0	+01 15 23.0	0.11700	11686	11036
MRC2251-178	MCG-03-58-009	22 54 05.9	-17 34 55.0	0.06609	12029	5515
MRK335	NGC7817	00 06 19.5	+20 12 11.0	0.02578	11524	5122
MRK771	NGC4529	12 32 03.6	+20 09 30.0	0.06301	12569	1868
MRK876	NGC6140	16 13 57.2	+65 43 11.0	0.12900	11524	12579
PG0804+761	UGC04238	08 10 58.7	+76 02 43.0	0.10200	11686	5510
PG1259+593	UGC08146	13 01 12.9	+59 02 07.0	0.4778 0	11541	9200
PG1302-102	NGC4939	13 05 33.0	-10 33 19.0	0.27840	12038	5979
QSO1500-4140	NGC5786	15 03 34.0	-41 52 23.0	0.33500	11659	9258
RBS1503	NGC5907	15 29 07.5	+56 16 07.0	0.09900	12276	1964
RBS1768	ESO343-G014	21 38 49.9	-38 28 40.0	0.18299	12936	6962
RBS2000	IC5325	23 24 44.7	-40 40 49.0	0.17359	13448	5046
RX_J1017.5+4702	NGC3198	10 17 31.0	+47 02 25.0	0.33544	13314	8655
RX_J1054.2+3511	NGC3432	10 54 16.2	+35 11 24.0	0.20300	14772	533
RX_J1117.6+5301	NGC3631	11 17 40.5	+53 01 51.0	0.15871	14240	4943
RX_J1121.2+0326	CGCG039-137, NGC3633	11 21 14.0	+03 25 47.0	0.15200	12248	2695
RX_J1142.7+4625	NGC3726	11 42 41.2	+46 24 36.0	0.11500	14772	2368
RX_J1236.0+2641	NGC4565	12 36 04.0	+26 41 36.0	0.20920	12248	4235
SBS1116+523	NGC3631	11 19 47.9	+52 05 53.0	0.35568	14240	4949
SBS1503+570	NGC5907	15 04 55.6	+56 49 20.0	0.35894	12276	5163
SDSSJ091052.80+333008.0	NGC2770	09 10 52.8	+33 30 08.0	0.11631	14240	7442
SDSSJ091127.30+325337.0	NGC2770	09 11 27.3	+32 53 37.0	0.29038	14240	10028
SDSSJ095914.80+320357.0	NGC3067	09 59 14.8	+32 03 57.0	0.56462	12603	2273
SDSSJ104335.90+115129.0	NGC3351	10 43 35.9	+11 05 29.0	0.79400	14071	4736
SDSSJ111443.70+525834.0	NGC3631	11 14 43.7	+52 58 34.0	0.07921	14240	13440
SDSSJ112439.50+113117.0	NGC3666	11 24 39.4	+11 31 17.0	0.14300	14071	10427
SDSSJ112448.30+531818.0	UGC06446, NGC3631	11 24 48.3	+53 18 19.0	0.53151	14240	7920
SDSSJ135726.27+043541.4	NGC5364	13 57 26.3	+04 35 41.0	1.23453	12264	14148
SDSSJ151237.15+012846.0	UGC09760	15 12 37.2	+01 28 46.0	0.26625	12603	7590
TON1009	NGC2770	09 09 06.2	+32 36 30.0	0.81028	12603	4740
TON1015	NGC2770	09 10 37.0	+33 29 24.0	0.35400	14240	4774

Note—Summary of COS targets in this sample.

Table 3 *(continued)*

#	Galaxy	Target	ρ (kpc)	Az. (Deg.)	v_{sys} ($\mathrm{km\,s^{-1}}$)	v_{rot} ($\mathrm{km\,s^{-1}}$)	$v_{\mathrm{Ly\alpha}}$ ($\mathrm{km\,s^{-1}}$)	$W_{\mathrm{Ly\alpha}}$ (mÅ)	Cyl. Model ($\mathrm{km\,s^{-1}}$)	NFW Model ($\mathrm{km\,s^{-1}}$)
(1)	(2)	(3)	(4)	(5)	(6)	(7)	(8)	(9)	(10)	(11)
5	NGC1566	1H0419-577	303	10	1502	86	1075	249	1550 - 1578	1500 - 1533
5	NGC1566	1H0419-577	303	10	1502	86	1123	269	1550 - 1578	1500 - 1533
5	NGC1566	1H0419-577	303	10	1502	86	1188	240	1550 - 1578	1500 - 1533
5	NGC1566	1H0419-577	303	10	1502	86	1264	91	1550 - 1578	1500 - 1533

Table 3 continued

Table 3 *(continued)*

#	Galaxy	Target	ρ	Az.	$v_{\rm sys}$	$v_{\rm rot}$	$v_{\rm Ly\alpha}$	$W_{\rm Ly\alpha}$	Cyl. Model	NFW Model
			(kpc)	(Deg.)	(km s^{-1})	(km s^{-1})	(km s^{-1})	(mÅ)	(km s^{-1})	(km s^{-1})
(1)	(2)	(3)	(4)	(5)	(6)	(7)	(8)	(9)	(10)	(11)
5	NGC1566	1H0419-577	303	10	1502	86	2020	9	1550 - 1578	1500 - 1533
6	NGC1566	HE0429-5343	256	60	1502	-86	1167	79	1449 - 1500	1480 - 1519
6	NGC1566	HE0429-5343	256	60	1502	-86	1358	136	1449 - 1500	1480 - 1519
7	NGC2770	FBQSJ0908+3246	204	59	1948	150	1915	202	1802 - 1944	1831 - 1958
7	NGC2770	FBQSJ0908+3246	204	59	1948	150	1982	230	1802 - 1944	1831 - 1958
8	NGC2770	TON1009	267	41	1948	150	1908	111	1802 - 1909	1838 - 1934
8	NGC2770	TON1009	267	41	1948	150	1980	243	1802 - 1909	1838 - 1934
9	NGC2770	TON1015	218	61	1948	150	1833	244	1951 - 2094	1938 - 2063
9	NGC2770	TON1015	218	61	1948	150	1985	80	1951 - 2094	1938 - 2063
10	NGC2770	SDSSJ091052.80+333008.0	239	66	1948	150	1824	266	1954 - 2093	1941 - 2060
10	NGC2770	SDSSJ091052.80+333008.0	239	66	1948	150	1975	68	1954 - 2093	1941 - 2060
11	NGC2770	SDSSJ091127.30+325337.0	234	30	1948	150	2063	271	1798 - 1905	1831 - 1929
12	NGC3067	3C232	11	74	1465	148.2	1408	2092	1344 - 1490	1326 - 1491
12	NGC3067	3C232	11	74	1465	148.2	1510	700	1344 - 1490	1326 - 1491
12	NGC3067	3C232	11	74	1465	148.2	1641	1635	1344 - 1490	1326 - 1491
13	NGC3067	SDSSJ095914.80+320357.0	128	43	1465	148.2	1493	623	1476 - 1603	1453 - 1546
14	NGC3198	RX_J1017.5+4702	370	55	660	152	629	71	507 - 639	569 - 666
15	NGC3351	SDSSJ104335.90+115129.0	31	43	778	198	717	823	679 - 790	710 - 798
15	NGC3351	SDSSJ104335.90+115129.0	31	43	778	198	882	621	679 - 790	710 - 798
15	NGC3351	SDSSJ104335.90+115129.0	31	43	778	198	1030	391	679 - 790	710 - 798
16	NGC3432	CSO295	20	82	616	122	600	568	579 - 664	579 - 750
16	NGC3432	CSO295	20	82	616	122	662	585	579 - 664	579 - 750
17	NGC3432	RX_J1054.2+3511	290	57	616	122	703	184	616 - 739	607 - 727
18	NGC3513	H1101-232	60	67	1204	20	1182	635	1185 - 1231	1185 - 1232
19	NGC3631	RX_J1117.6+5301	78	75	1156	145	1131	374	1166 - 1180	1157 - 1177
19	NGC3631	RX_J1117.6+5301	78	75	1156	145	1259	62	1166 - 1180	1157 - 1177
20	NGC3631	SBS1116+523	163	40	1156	145	-99	-99	1100 - 1151	1125 - 1167
21	NGC3631	SDSSJ111443.70+525834.0	145	72	1156	145	1163	232	1164 - 1185	1151 - 1180
22	NGC3631	SDSSJ112448.30+531818.0	86	74	1156	145	1019	71	1130 - 1145	1134 - 1157
22	NGC3631	SDSSJ112448.30+531818.0	86	74	1156	145	1141	165	1130 - 1145	1134 - 1157
23	NGC3633	RX_J1121.2+0326	184	58	2587	-157	2605	180	2434 - 2573	2510 - 2597
24	NGC3666	SDSSJ112439.50+113117.0	58	83	1060	131.8	1047	345	973 - 1080	924 - 1080
24	NGC3666	SDSSJ112439.50+113117.0	58	83	1060	131.8	1099	272	973 - 1080	924 - 1080
25	NGC3726	CSO1208	369	88	866	167.2	731	470	839 - 895	838 - 887
25	NGC3726	CSO1208	369	88	866	167.2	874	506	839 - 895	838 - 887
26	NGC3726	RX_J1142.7+4625	440	86	866	167.2	818	375	832 - 852	836 - 859
27	NGC4529	MRK771	159	23	2536	106.4	2553	240	2433 - 2496	2449 - 2511
28	NGC4536	3C273.0	349	11	1867	139	1580	369	1954 - 1988	1872 - 1908
28	NGC4536	3C273.0	349	11	1867	139	2156	42	1954 - 1988	1872 - 1908
28	NGC4536	3C273.0	349	11	1867	139	2267	27	1954 - 1988	1872 - 1908
29	NGC4536	HE1228+0131	338	51	1867	139	1495	160	1885 - 1918	1869 - 1899
29	NGC4536	HE1228+0131	338	51	1867	139	1571	23	1885 - 1918	1869 - 1899
29	NGC4536	HE1228+0131	338	51	1867	139	1686	321	1885 - 1918	1869 - 1899
29	NGC4536	HE1228+0131	338	51	1867	139	1721	303	1885 - 1918	1869 - 1899
29	NGC4536	HE1228+0131	338	51	1867	139	1854	78	1885 - 1918	1869 - 1899
30	NGC4565	RX_J1236.0+2641	147	41	1230	253	1009	365	1228 - 1476	1200 - 1374
30	NGC4565	RX_J1236.0+2641	147	41	1230	253	1166	305	1228 - 1476	1200 - 1374
30	NGC4565	RX_J1236.0+2641	147	41	1230	253	1254	122	1228 - 1476	1200 - 1374
31	NGC4939	PG1302-102	254	61	3093	-275	3448	72	2874 - 3107	2974 - 3129
32	NGC5364	SDSSJ135726.27+043541.4	165	84	1238	55	967	348	1212 - 1346	1208 - 1306
32	NGC5364	SDSSJ135726.27+043541.4	165	84	1238	55	1124	83	1212 - 1346	1208 - 1306
33	NGC5786	QSO1500-4140	453	1	2975	172	3138	177	3081 - 3135	2994 - 3042

Table 3 continued

Table 3 *(continued)*

#	Galaxy	Target	ρ	Az.	$v_{\rm sys}$	$v_{\rm rot}$	$v_{\rm Ly\alpha}$	$W_{\rm Ly\alpha}$	Cyl. Model	NFW Model
			(kpc)	(Deg.)	(km s^{-1})	(km s^{-1})	(km s^{-1})	(mÅ)	(km s^{-1})	(km s^{-1})
(1)	(2)	(3)	(4)	(5)	(6)	(7)	(8)	(9)	(10)	(11)
34	NGC5907	SBS1503+570	413	47	667	227.4	708	301	698 - 895	643 - 768
35	NGC5907	RBS1503	478	63	667	227.4	-99	-99	439 - 658	571 - 700
36	NGC5951	2E1530+1511	55	85	1780	127.9	1795	507	1749 - 1894	1748 - 1905
36	NGC5951	2E1530+1511	55	85	1780	127.9	1953	137	1749 - 1894	1748 - 1905
37	NGC6140	MRK876	113	21	910	138.11	939	379	950 - 1011	945 - 1012
38	NGC7817	MRK335	343	90	2309	180.4	1954	216	2283 - 2285	2283 - 2285
38	NGC7817	MRK335	343	90	2309	180.4	2274	150	2283 - 2285	2283 - 2285
39	UGC04238	PG0804+761	148	59	1544	91.6	1526	62	1541 - 1630	1534 - 1619
39	UGC04238	PG0804+761	148	59	1544	91.6	1593	32	1541 - 1630	1534 - 1619
40	UGC06446	SDSSJ112448.30+531818.0	143	22	645	79.4	664	339	636 - 710	630 - 706
41	UGC08146	PG1259+593	114	50	670	82.4	646	133	657 - 752	654 - 753
41	UGC08146	PG1259+593	114	50	670	82.4	683	168	657 - 752	654 - 753
42	UGC09760	SDSSJ151237.15+012846.0	123	90	2094	-46	2029	506	2064 - 2124	2064 - 2180

Note—Comments.

4. DISCUSSION

We have presented data on XXXX QSO-galaxy systems, representing XXXX individual Lyα-galaxy matchups, for which we have galaxy information including kinematics, inclination, size and luminosity. This is the largest sample of this kind to date and provides the best yet opportunity to study the kinematic connection between galaxies and their neutral H I halos. Table 4 summarizes our galaxy-absorber sample and the predicted velocity range given by each model for co-rotation.

In this section we consider in aggregate our sample of Lyα absorbers, and the fraction consistent with co-rotation under various cuts and constraints.

To start we consider the fraction of absorbers which appear to be rotating in the same sense as the nearby galaxy. With no cuts of any kind, we find 46% of absorbers have velocities of the "correct" sign (versus 35% "incorrect") to be rotating in the same sense as the nearby galaxies. However, many of these absorbers have a velocity difference, Δv, larger than the inclination-corrected galaxy rotation velocity (v_{rot}). This results in a much smaller fraction of co-rotating absorbers when compared to our cylindrical and NFW profile models (28% and 29%, respectively), which will never output an absorber velocity higher than v_{rot}. In undertaking this study we are assuming that absorption within some velocity limit and impact parameter from a galaxy is likely associated with that galaxy. To start with we set these limits at $\Delta v_{max} = 400$ km s^{-1} and $\rho_{max} = 3R_{vir}$.

Let us now instead consider only absorbers with $\Delta v \leq v_{rot} \pm 10$ km s^{-1}, or absorbers with velocities differences no greater than the maximal galaxy rotation velocity ($\pm$ a 10 km s^{-1} buffer to account for velocity uncertainties). With this constraint the co-rotating fraction increases to 50%.[2] One additional constraining step we take is to only consider galaxies which have no neighbors within at least 20 kpc. The disruptions caused by near neighbors to both galaxy H I disks and halos has been well established observationally, so a 20 kpc minimum separation should at least remove the systems most likely to be disrupted. This constraint alone leads to a co-rotating fraction of 40%. Combining both constraints results in a 54% co-rotating fraction.

Next, we consider the effect of galaxy luminosity. We separate our sample about 0.5 L^*, while keeping our $\Delta v \leq v_{rot} \pm 10$ km s^{-1}constraint and relaxing the 20 kpc nearest-neighbor criteria in order to maximize the sample size. This results in 10 absorbers near $L \leq 0.5L^*$ galaxies and 34 around more luminous galaxies. The co-rotating fraction around luminous galaxies is then 32%, compared to 100% around $L \leq 0.5L^*$ galaxies. In fact, the co-rotating absorber fraction smoothly decreases as a function of L^*, as shown in Figure 3.

Finally, we consider the Doppler b-parameters of our absorber sample. Figure 5 shows the distribution of b-parameters for all Lyα absorbers with $v_{Ly\alpha} \leq v_{rot} \pm 10$ km s^{-1}. In the top panel we separate them into co-rotating and anti-rotating subsets, in the middle panel we do the same but only for $\rho \leq 1R_{vir}$, and on the bottom we separate based on absorbers near $L^* \leq 0.5$ and $L^* > 0.5$ galaxies. Interestingly, we find that *higher* b-parameter absorbers tend to be both co-rotating and found near $L^* \leq 0.5$ galaxies. The picture described by Stewart et al. (2011b), however, **FIND MORE AND NEWER CITATIONS** describes a scenario where co-rotating gas is predominately the product of cold-mode

[2] From here on we concentrate on the results using our NFW profile model. The cylindrical model results do not differ in a systematically interesting way.

Table 4. Results

Sub-sample	Co-rotating	Anti-rotating	Uncertain	Co-rotating $\rho \leq 1$	Anti-rotating $\rho \leq 1$	Co-rotating $\rho > 1$	Anti-rotating $\rho > 1$
Apparent Vel.	30	26	9	13	9	17	17
Cyl. Model	22	34	9	9	13	13	21
NFW Model	24	32	9	9	13	15	19
NFW w/ Constraint: $v_{Ly\alpha} \leq v_{rot}$	24	14	5	9	6	15	8
NFW w/ Constraint: Nearest $\rho \geq 20$ kpc	13	13	6	3	3	10	10
NFW w/ Both Constraints	13	8	2	3	1	10	7
NFW w/ v_{rot} Constraint: $[0 \leq L^* \leq 0.5]$	10	1	0	5	1	5	0
NFW w/ v_{rot} Constraint $[L^* > 0.5]$	14	13	5	4	5	10	8

Note—Comments.

accretion. Hotter, outflowing gas would likely carry angular momentum from the disk with it, but this would be quickly lost as the outflows expand into the halo and result in negligible observable rotation. In Figure 4 we show how the b-parameters vary as a function of Δv for co-rotating versus anti-rotating absorbers. We would expect the co-rotating sample to occupy a narrower Δv space based on their definition (Δv fitting within the velocity bounds given by our model), but the elevated b-parameters for these compared to the relatively flat distribution for anti-rotators is intriguing.

Lutz et al. (2018) find that galaxies with high H Imass compared to their stellar mass have higher halo angular momentum, which may be impeding their ability to efficiently form stars. While we do not have independent measures of H Iand stellar mass for our galaxies, it may not be unreasonable to think that these high angular momentum galaxies reside toward the lower luminosity end of our sample.

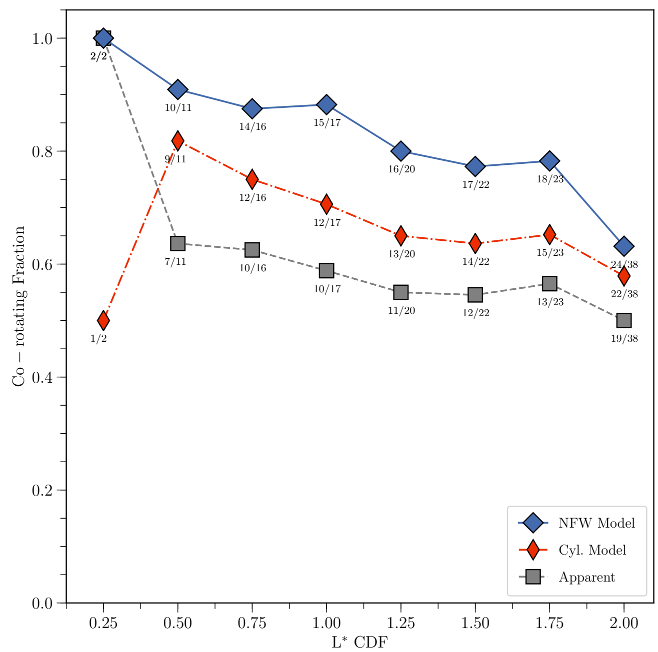

Figure 2. The fraction of co-rotating absorbers as a function of cumulative L^* distribution. All systems are included at L^*=1.6 (this bin includes galaxies brighter than 1.6L^* as well), then only galaxies with $L^* \leq 1.4$ are included at L^* =1.4, and so on.

5. SUMMARY

D. M. F. thanks Claire Murray for useful insights on our halo model, and Julie Davis for invaluable SALT data reduction pointers. This research has made use of the NASA/IPAC Extragalactic Database (NED) which is operated by the Jet Propulsion Laboratory, California Institute of Technology, under contract with the National Aeronautics and Space Administration. Based on observations with the NASA/ESA *Hubble Space Telescope*, obtained at the Space Telescope Science Institute (STScI), which is operated by the Association of Universities for Research in Astronomy, Inc., under NASA contract NAS 5-26555. **SALT ACKNOWLEDGEMENT**. Spectra were retrieved from the Barbara A. Mikulski Archive for Space Telescopes (MAST) at STScI. Over the course of this study, D.M.F. and B.P.W. were supported by grant AST-1108913, awarded by the US National Science Foundation, and by NASA grants *HST*-AR-12842.01-A, *HST*-AR-13893.01-A, and *HST*-GO-14240 (STScI).

Facility: HST (COS), SALT (RSS)

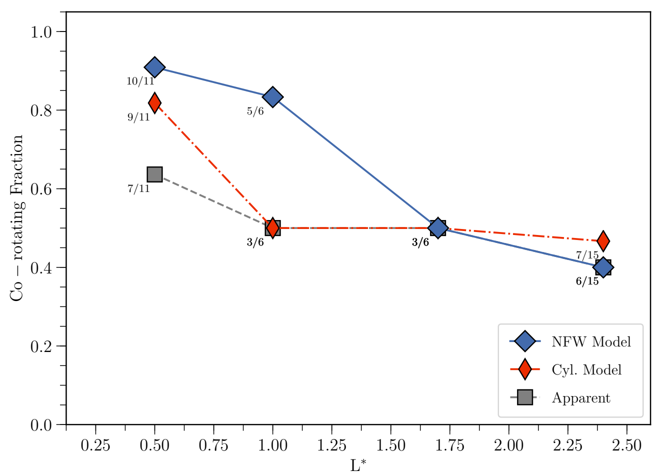

Figure 3. The fraction of co-rotating absorbers as a function of L^*. The upper edges of the L^* bins are located at 0.5, 1.0, 1.7, and > 1.7 L^* (i.e., all systems $1.7L^*$ and higher)

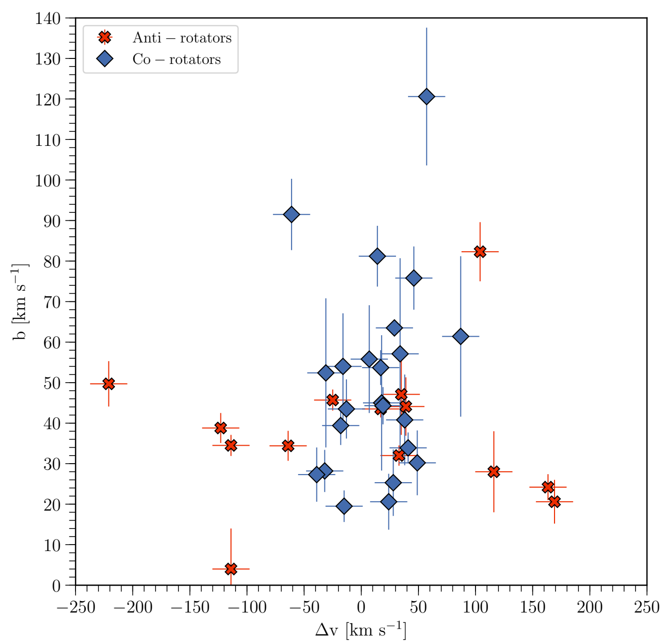

Figure 4. The Doppler b-parameters of each absorber as a function of Δv, split into co-rotating (blue diamonds) and anti-rotating (red crosses). The data point for the NGC3067-3C232 LLS ($b = 245.2 \pm 25.9$, $\Delta v = -68.0 \pm 11$ $\mathrm{km\,s^{-1}}$) is not shown in order to highlight the majority distribution in greater detail.

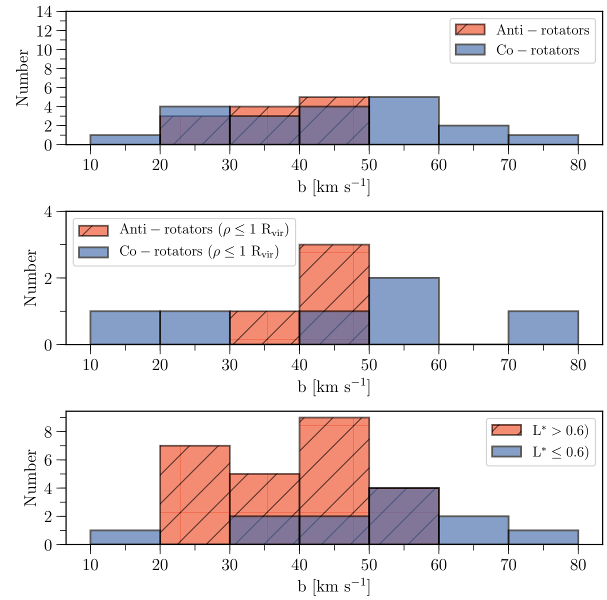

Figure 5. Histograms showing the distributions of Doppler b-parameters for all Lyα absorbers with $v_{Ly\alpha} \leq v_{rot} \pm 10$ $\mathrm{km\,s^{-1}}$. In the top panel we separate them into co-rotating (blue) and anti-rotating (red-hatched) subsets based on our NFW model results, in the middle we do the same but only for $\rho \leq 1R_{vir}$, and on the bottom we separate based on absorbers near $L^* \leq 0.5$ (blue) and $L^* > 0.5$ (red-hatched) galaxies.

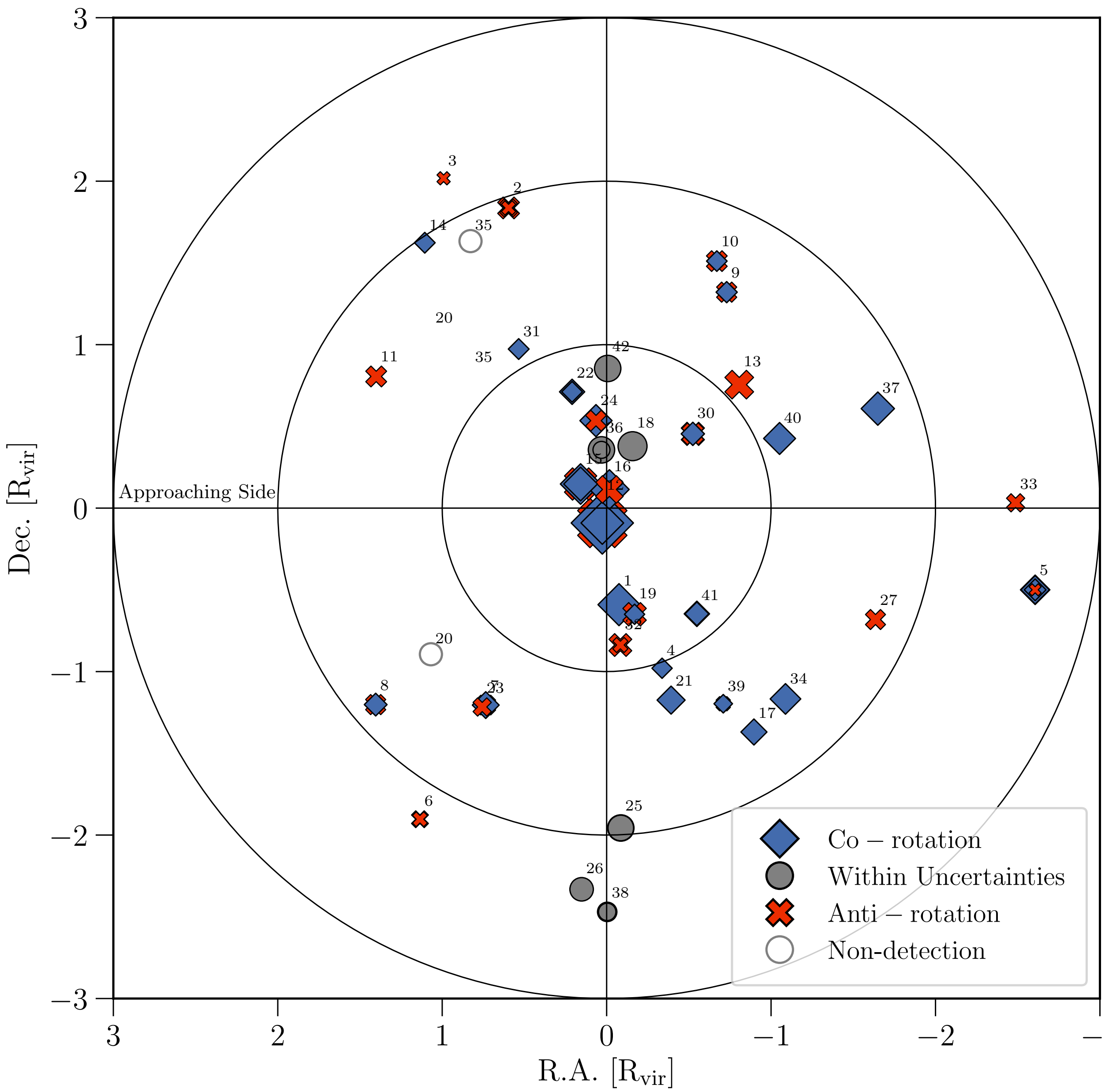

Figure 6. A map of the locations of each absorber normalized with respect to the galaxy virial radius. The color and style of each point indicates the line-of-sight velocity compared to that of the rotation of the nearby galaxy. Blue diamonds indicate co-rotation, red crosses indicate anti-rotation, and grey circles indicate cases where either is possible due to a combination of orientation and velocity uncertainties. The size of each point is scaled to reflect the EW of the absorber. Concentric rings indicate distances of 1, 2, and 3 $R_{\rm vir}$. All galaxies are rotated to PA = 90 or 270, such that their major axis' are horizontal and their approaching side is on the left as indicated. The number identifiers correspond to the system number given in column (1) of Table 3.

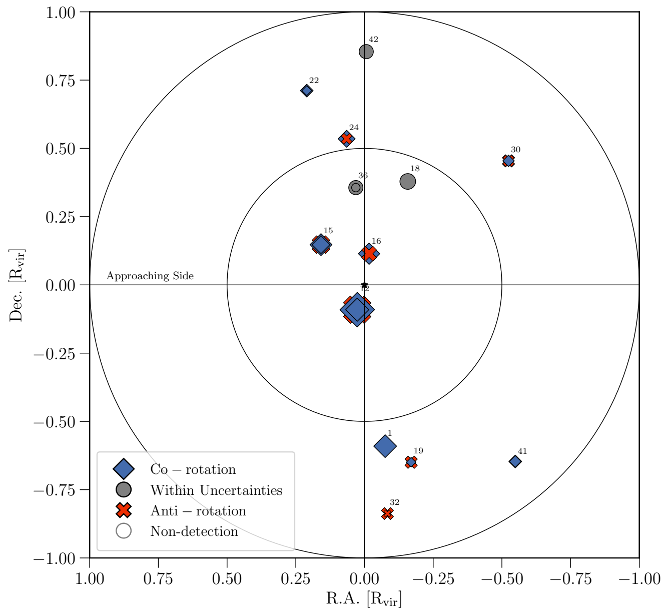

Figure 7. A map of the locations of each absorber normalized with respect to the galaxy virial radius, showing only those systems within $1R_{\rm vir}$. The color and style of each point indicates the line-of-sight velocity compared to that of the rotation of the nearby galaxy. Blue diamonds indicate co-rotation, red crosses indicate anti-rotation, and grey circles indicate cases where either is possible due to a combination of orientation and velocity uncertainties. The size of each point is scaled to reflect the EW of the absorber. Concentric rings indicate distances of 0.5 and 1 R_{vir}. All galaxies are rotated to PA = 90 or 270, such that their major axis' are horizontal and their approaching side is on the left as indicated. The number identifiers correspond to the system number given in column (1) of Table 3.

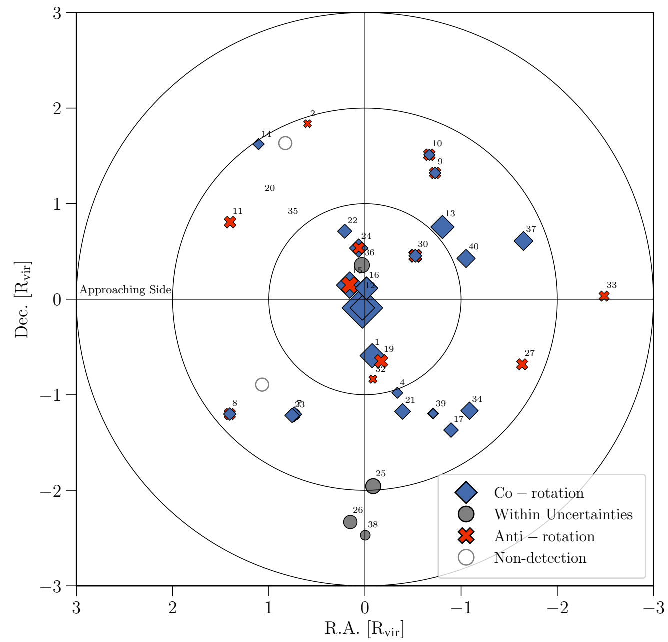

Figure 8. A map of the locations of each absorber normalized with respect to the galaxy virial radius. The color and style of each point indicates the NFW rotation model results for each absorber with a $v_{\rm Ly\alpha} \leq v_{\rm rot}$ constraint imposed. Blue diamonds indicate co-rotation, red crosses indicate anti-rotation, and grey circles indicate cases where either is possible due to a combination of orientation and velocity uncertainties. The size of each point is scaled to reflect the EW of the absorber. Concentric rings indicate distances of 1, 2, and 3 R_{vir}. All galaxies are rotated to PA = 90 or 270, such that their major axis' are horizontal and their approaching side is on the left as indicated. The number identifiers correspond to the system number given in column (1) of Table 3.

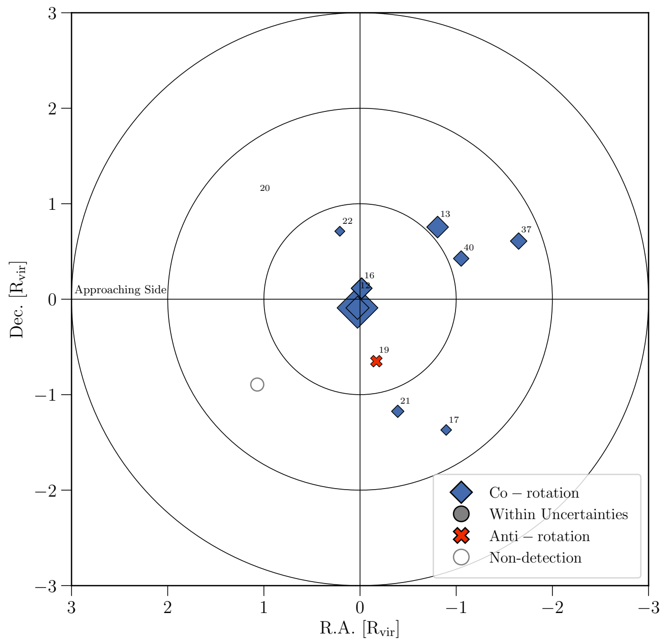

Figure 9. A map of the locations of each absorber normalized with respect to the galaxy virial radius. The color and style of each point indicates the NFW rotation model results for each absorber with $v_{Ly\alpha} \leq v_{rot}$ and $[L^* > 0.5]$ constraints imposed. Blue diamonds indicate co-rotation, red crosses indicate anti-rotation, and grey circles indicate cases where either is possible due to a combination of orientation and velocity uncertainties. The size of each point is scaled to reflect the EW of the absorber. Concentric rings indicate distances of 1, 2, and 3 R_{vir}. All galaxies are rotated to PA = 90 or 270, such that their major axis' are horizontal and their approaching side is on the left as indicated. The number identifiers correspond to the system number given in column (1) of Table 3.

REFERENCES

Abazajian, K., Adelman-McCarthy, J. K., Agüeros, M. A., et al. 2005, AJ, 129, 1755

Bowen, D. V., Chelouche, D., Jenkins, E. B., et al. 2016, ApJ, 826, 50

Brook, C. B., Governato, F., Roškar, R., et al. 2011, MNRAS, 415, 1051

Carilli, C. L., van Gorkom, J. H., & Stocke, J. T. 1989, Nature, 338, 134

Charlton, J. C., & Churchill, C. W. 1998, ApJ, 499, 181

Chen, D. N., Jing, Y. P., & Yoshikaw, K. 2003, ApJ, 597, 35

Corwin, Jr., H. G., Buta, R. J., & de Vaucouleurs, G. 1994, AJ, 108, 2128

Côté, S., Wyse, R. F. G., Carignan, C., Freeman, K. C., & Broadhurst, T. 2005, ApJ, 618, 178

Danovich, M., Dekel, A., Hahn, O., & Teyssier, R. 2012, MNRAS, 422, 1732

de Blok, W. J. G., Walter, F., Brinks, E., et al. 2008, AJ, 136, 2648

di Nella, H., Paturel, G., Walsh, A. J., et al. 1996, A&AS, 118, 311

Diamond-Stanic, A. M., Coil, A. L., Moustakas, J., et al. 2016, ApJ, 824, 24

Dicaire, I., Carignan, C., Amram, P., et al. 2008, MNRAS, 385, 553

Falco, E. E., Kurtz, M. J., Geller, M. J., et al. 1999, PASP, 111, 438

French, D. M., & Wakker, B. P. 2017, ApJ, 837, 138

Giovanelli, R., Avera, E., & Karachentsev, I. D. 1997, AJ, 114, 122

Green, J. C., Froning, C. S., Osterman, S., et al. 2012, ApJ, 744, 60

Grogin, N. A., Geller, M. J., & Huchra, J. P. 1998, ApJS, 119, 277

Jones, D. H., Read, M. A., Saunders, W., et al. 2009, MNRAS, 399, 683

Keeney, B. A., Momjian, E., Stocke, J. T., Carilli, C. L., & Tumlinson, J. 2005, ApJ, 622, 267

Kimm, T., Slyz, A., Devriendt, J., & Pichon, C. 2011, MNRAS, 413, L51

Knapen, J. H. 1997, MNRAS, 286, 403

Koribalski, B. S., Staveley-Smith, L., Kilborn, V. A., et al. 2004, AJ, 128, 16

Lu, N. Y., Hoffman, G. L., Groff, T., Roos, T., & Lamphier, C. 1993, ApJS, 88, 383

Lutz, K. A., Kilborn, V. A., Koribalski, B. S., et al. 2018, MNRAS, 476, 3744

Mathewson, D. S., & Ford, V. L. 1996, ApJS, 107, 97

Navarro, J. F., Frenk, C. S., & White, S. D. M. 1996, ApJ, 462, 563

—. 1997, ApJ, 490, 493

Pichon, C., Pogosyan, D., Kimm, T., et al. 2011, MNRAS, 418, 2493

Rhee, M.-H., & van Albada, T. S. 1996, A&AS, 115, 407

Rubin, V. C., Thonnard, N. T., & Ford, Jr., W. K. 1982, AJ, 87, 477

Sharma, S., & Steinmetz, M. 2005, ApJ, 628, 21

Shen, S., Madau, P., Guedes, J., et al. 2013, ApJ, 765, 89

Sofue, Y. 1996, ApJ, 458, 120

Steidel, C. C., Kollmeier, J. A., Shapley, A. E., et al. 2002, ApJ, 570, 526

Stewart, K. R., Brooks, A. M., Bullock, J. S., et al. 2013, ApJ, 769, 74

Stewart, K. R., Kaufmann, T., Bullock, J. S., et al. 2011a, ApJL, 735, L1

—. 2011b, ApJ, 738, 39

Stewart, K. R., Maller, A. H., Oñorbe, J., et al. 2017, ApJ, 843, 47

Stocke, J. T., Keeney, B. A., & Danforth, C. W. 2010, PASA, 27, 256

Swaters, R. A., Sancisi, R., van Albada, T. S., & van der Hulst, J. M. 2009, A&A, 493, 871

Verheijen, M. A. W., & Sancisi, R. 2001, A&A, 370, 765

Wakker, B. P., Hernandez, A. K., French, D. M., et al. 2015, ApJ, 814, 40

Wakker, B. P., & Savage, B. D. 2009, ApJS, 182, 378

Yim, K., Wong, T., Xue, R., et al. 2014, AJ, 148, 127

APPENDIX

A. GALAXY SAMPLE

B. SALT GALAXIES

In this section we summarize each galaxy-QSO system observed by SALT. We calculate impact parameters to QSOs and galaxy-absorber velocity separations ($\Delta v = v_{\mathrm{Ly}\alpha} - v_{\mathrm{sys}}$) based on our measured v_{sys} values. Both measured and previously published values for v_{sys} are given in Table 1 for reference. We provide rotation curves and finder chart images for the sub-sample of galaxies with newly observed SALT data.

B.1. *CGCG039-137*

CGCG039-137 is an isolated Scd type galaxy with a measured systemic velocity $v_{\mathrm{sys}} = 6918 \pm 24$ km s^{-1} and inclination of $i = 63°$. The QSO RX_J1121.2+0326 is located nearby at an impact parameter of 99 kpc and azimuth angle of 71° on the receding side. The data for RX_J1121.2+0326 has low signal-to-noise (~ 4.2), but we are able to detect Lyα at 6975 km s^{-1} , which, at $\Delta v = 57$ km s^{-1}, lies well within the range of projected velocities consistent with co-rotation (cylindrical model = [-36, 137], NFW = [-37, 164] km s^{-1}).

B.2. *ESO343-G014*

ESO343-G014 is an edge-on spiral galaxy with a measured systemic velocity $v_{\mathrm{sys}} = 9139\pm$ 32 km s^{-1}. It has a smaller neighboring galaxy, 2MASXJ21372816-3824412, located north of it's major axis at a projected distance of 216 kpc and velocity of 9129 km s^{-1}. The nearest sightline is towards RBS1768 at $\rho = 466$ kpc and 74° azimuth angle on the approaching side. We detect 3 blended Lyα absorption components toward RBS1768 at $v_{\mathrm{Ly}\alpha} = 9308, 9360, 9434$ km s^{-1} ($\Delta v = 169, 221, 295$ km s^{-1}). This system is highly blended and contaminated with galactic S I, and therefore their widths are not reliable. All of these are anti-aligned with the rotation of ESO343-G014 relative to the models (cylindrical = [-203, 10], NFW = [-122, 31] km s^{-1}). Unfortunately the presence of 2MASXJ21372816-3824412 makes it difficult to attribute this gas solely to ESO343-G014. Additionally, this gas could be attributed to either the approaching or receding side of the disk due to the large impact parameter and high azimuth angle of the sightline.

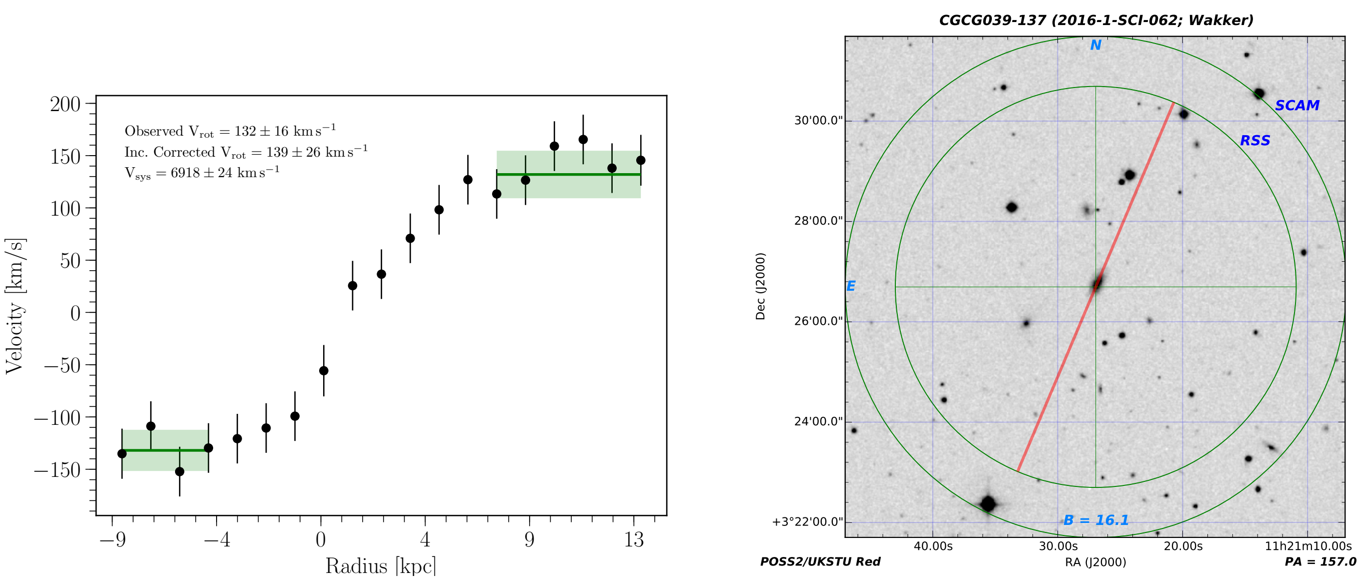

(a) (b)

Figure 10. a) Rotation curve of CGCG039-137. The solid green line indicates the weighted mean velocity over the corresponding x-axis region, and the shaded green indicates the 1σ error in the mean. b) SALT finder chart for CGCG039-137 showing the position of the slit in red.

B.3. *IC5325*

IC5325 is a mostly face-on SAB(rs)bc type galaxy with a measured systemic velocity $v_{\mathrm{sys}} = 1512 \pm 8$ km s^{-1}. It's inclination is just high enough ($i = 25°$) to obtain a reasonable rotation curve. The closest neighboring galaxy is

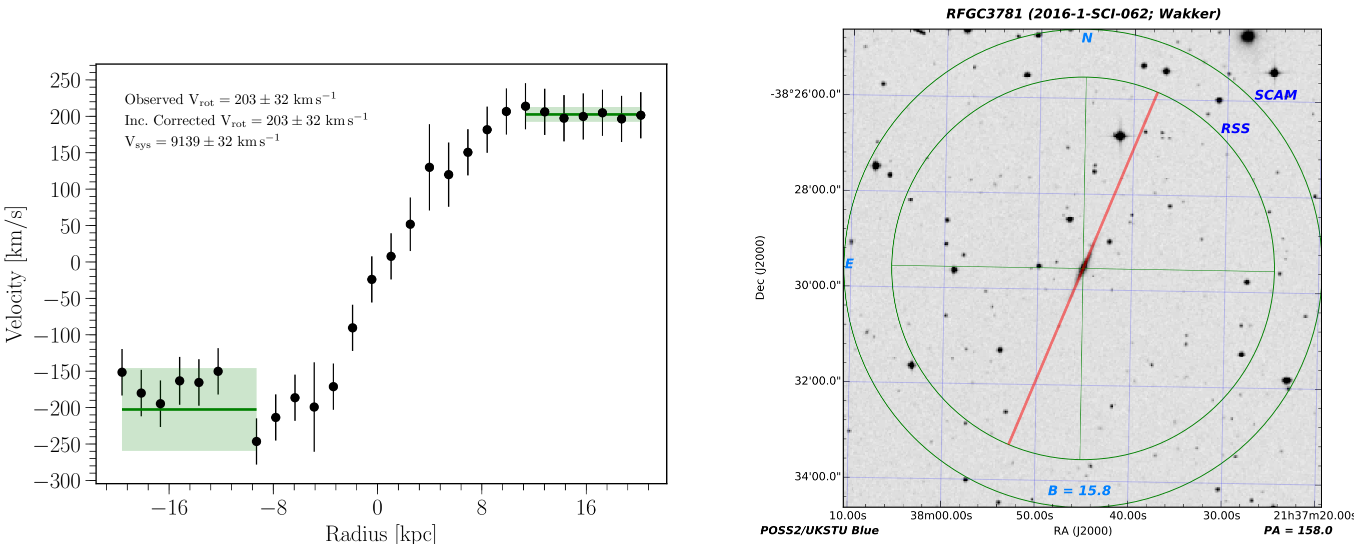

(a) (b)

Figure 11. a) Rotation curve of ESO343-G014. The solid green line indicates the weighted mean velocity over the corresponding x-axis region, and the shaded green indicates the 1σ error in the mean. b) SALT finder chart for ESO343-G014 showing the position of the slit in red.

ESO347-G020 to the southeast at 306 kpc and $v_{sys} = 1745$ km s^{-1}. Three other much smaller galaxies are also located ~ 450 kpc to the southwest. The background QSO RBS2000 is located northeast at $\rho = 314$ kpc and 64° azimuth angle on the approaching side of IC5325. We detect Lyα at $v_{\mathrm{Ly}\alpha} = 1598$ km s^{-1} ($\Delta v = 86$ km s^{-1}) towards RBS2000. While this velocity is anti-aligned with the rotation the disk gas relative to our model predictions (cylindrical = [-41, -20], NFW = [-29, 1] km s^{-1}), the low inclination angle of IC5325 leads to a highly uncertain position angle. Without additional observations, we cannot say for certain if the location of RBS2000 actually lies on the approaching or receding side. This position angle uncertainty also means our SALT rotation curve is a lower limit on the true rotation velocity of IC5325.

B.4. *MCG-03-58-009*

MCG-03-58-009 is a massive and very isolated Sc type galaxy at a measured systemic velocity of $v_{\mathrm{sys}} = 9015 \pm 19$ km s^{-1} and inclination angle of $i = 49°$. The background QSO MRC2251-178 is located southeast at $\rho = 355$ kpc at an azimuth angle of 71° on the receding side. We detect a weak Lyα absorber at $v_{\mathrm{Ly}\alpha} = 9029$ km s^{-1} ($\Delta v = 14$ km s^{-1}) towards MRC2251-178. This absorber velocity falls well within the expected range for co-rotation relative to our models (cylindrical = [-26, 137], NFW = [-42, 83] km s^{-1}). Although this absorber matches the velocity expected for co-rotation, the velocity difference ($\Delta v = 14$ km s^{-1}) is also within the systemic velocity uncertainty for MCG-03-58-009. The relative weakness of this absorber (EW = 62 ± 4 mÅ) is somewhat unusual given it's proximity (just outside of 1 R_{vir}) to a massive galaxy. If this is representative of an isolated system such as MCG-03-58-009, then we should expect the halo rotational velocity to approach systemic by 1 R_{vir}.

B.5. *NGC1566*

NGC1566 is a SAB(rs)bc type galaxy with measured systemic velocity of $v_{\mathrm{sys}} = 1502 \pm 15$ km s^{-1} and inclination angle of $i = 46°$. There are several other large galaxies at $\rho \gtrsim 200$ kpc from NGC1566 (e.g., NGC1549, NGC1596, and NGC1581). The closest QSO sightline is toward HE0429-5343, northeast of NGC1566 at $\rho = 256$ kpc and 60° azimuth angle. We detect Lyα absorption toward HE0429-5343 at $v_{\mathrm{Ly}\alpha} = 1167, 1358$ km s^{-1} ($\Delta v = -335, -144$ km s^{-1}). Both of these absorbers have the correct velocity *sign*, but we would expect a smaller velocity for co-rotation based on our model results (cylindrical = [-53, -2], NFW = [-22, 17] km s^{-1}). Unfortunately NGC1617 is slightly closer to this sightline than NGC1566, at $\rho = 233$ kpc and $v_{\mathrm{sys}} = 1063$ km s^{-1}, so it is not possible to confidently attribute these absorbers to NGC1566.

A more distant QSO sightline toward 1H0419-577 is located to the south at $\rho = 303$ kpc and just east of the receding side of the major axis at an azimuth angle of 10°. We detect Lyα at $v_{\mathrm{Ly}\alpha} = 1123, 1188, 1264$ km s^{-1} ($\Delta v = -379, -314, -238$ km s^{-1}), all of which are the wrong sign for co-rotation relative to our models (cylindrical = [48, 76], NFW = [-2, 31] km s^{-1}). This sightline is *also* actually closer to a small group of galaxies including NGC1549,

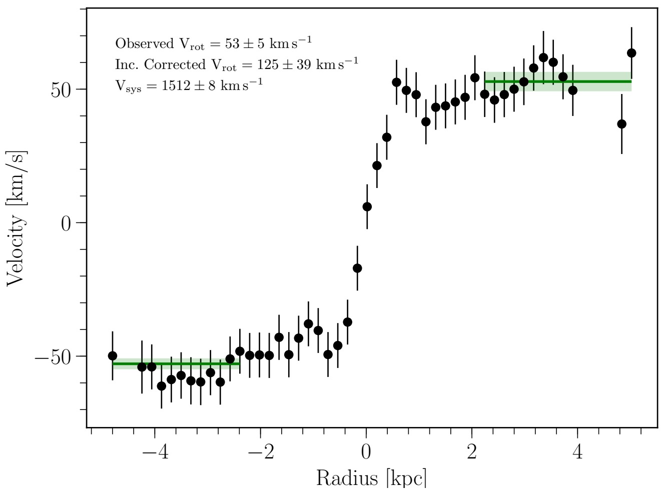

(a)

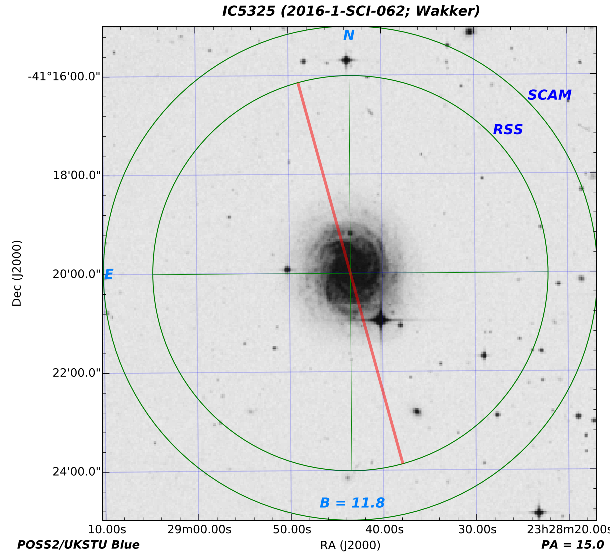

(b)

Figure 12. a) Rotation curve of IC5325. The solid green line indicates the weighted mean velocity over the corresponding x-axis region, and the shaded green indicates the 1σ error in the mean. b) SALT finder chart for IC5325 showing the position of the slit in red.

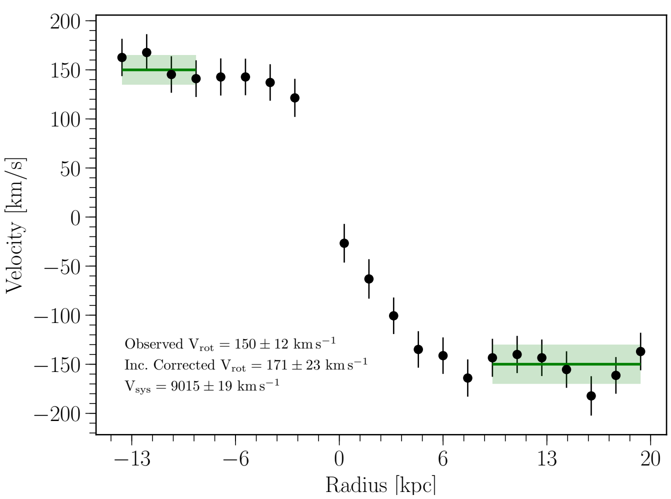

(a)

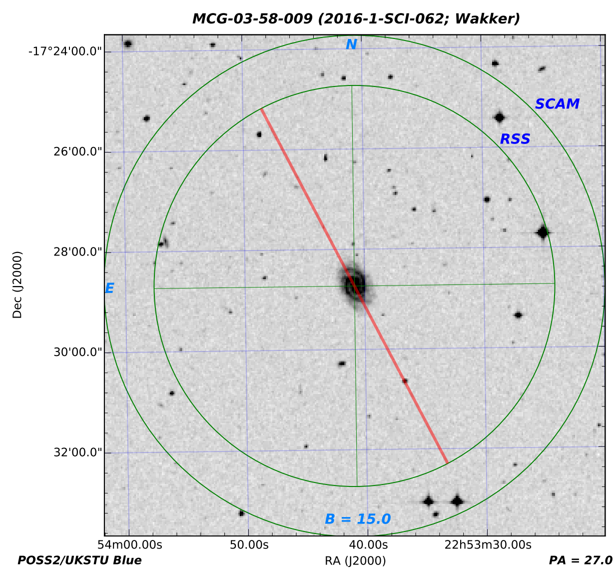

(b)

Figure 13. a) Rotation curve of MCG-03-58-009. The solid green line indicates the weighted mean velocity over the corresponding x-axis region, and the shaded green indicates the 1σ error in the mean. b) SALT finder chart for MCG-03-58-009 showing the position of the slit in red.

NGC1546 and NGC1536, all with systemic velocities near ~ 1200 km s^{-1}. Additionally, this absorber system contains C III, C IV, Si II, Si III, Si IV lines. These lines likely are associated with this group rather than with NGC1566.

B.6. *NGC3513*

NGC3513 a mostly face-on SB(rs)c galaxy with measured systemic velocity $v_{sys} = 1204 \pm 12$ km s^{-1}. It has a companion galaxy in NGC3511 at $\rho = 44$ kpc and $v_{sys} = 1109$ km s^{-1} (NGC3513 diameter $D = 22.1$ kpc, NGC3511 diameter $D = 28.1$ kpc). The background QSO H1101-232 is located directly south of the pair at $\rho = 60$ kpc and azimuth angle of 67° on the receding side. We detect Lyα at $v_{\mathrm{Ly}\alpha} = 1182\ \mathrm{km\,s^{-1}}$ ($\Delta v = -22\ \mathrm{km\,s^{-1}}$) toward H1101-232. NGC3513 appears to be rotating slowly, with a maximal inclination-corrected rotation velocity of $v_{\mathrm{rot}}/\sin(i) = 22 \pm 24$ $\mathrm{km\,s^{-1}}$. The $\Delta v = -22\ \mathrm{km\,s^{-1}}$ for this absorber matches well with the magnitude of this rotation, but is opposite in sign for co-rotation on the sky and just outside our predicted model velocity range (cylindrical = [-19, 27], NFW = [-19, 28] $\mathrm{km\,s^{-1}}$). Given that NGC3511 is so close, this absorber's velocity is probably subject to a complex velocity field influenced by both NGC3511 and NGC3513. This absorber system also contains C IV, N V, Si II, Si III, and Si IV lines.

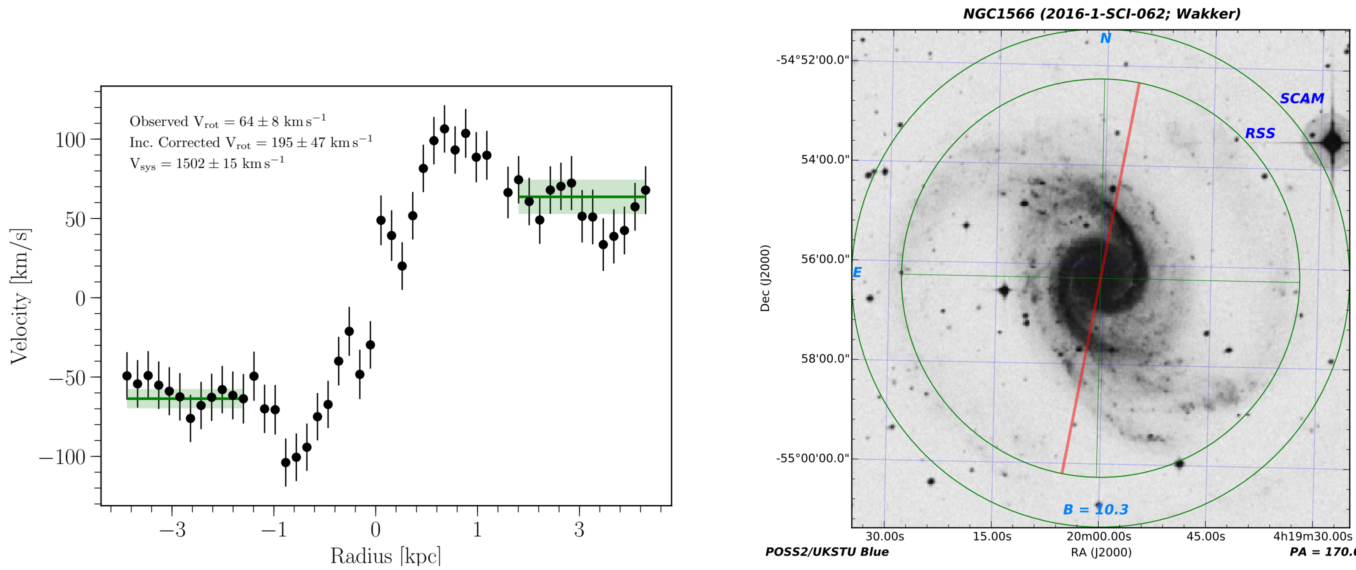

(a) (b)

Figure 14. a) Rotation curve of NGC1566. The solid green line indicates the weighted mean velocity over the corresponding x-axis region, and the shaded green indicates the 1σ error in the mean. b) SALT finder chart for NGC1566 showing the position of the slit in red.

B.7. *NGC3633*

NGC3633 is an isolated, edge-on SAa type galaxy with a measured systemic velocity $v_{\mathrm{sys}} = 2587 \pm 7\ \mathrm{km\,s^{-1}}$. Several locations along the disk of NGC3633 show two velocities for emission. We have combined these into a single velocity measurement via a weighted average.

The background QSO RX_J1121.2+0326 is located southeast at $\rho = 184$ kpc and 58° azimuth on the approaching side of NGC3633. We detect Lyα at $v_{\mathrm{Ly}\alpha} = 2605\ \mathrm{km\,s^{-1}}$ ($\Delta v = 18\ \mathrm{km\,s^{-1}}$) toward RX_J1121.2+0326. While close to v_{sys}, this absorber velocity is just outside our predicted model velocities (cylindrical = [-153, -14], NFW = [-77, 10] $\mathrm{km\,s^{-1}}$). However, this absorber is also very weak and broad, making the velocity center uncertain by at least ~ 10 $\mathrm{km\,s^{-1}}$. Taking this along with the uncertainty in V_{sys}, this absorber could still be consistent with co-rotation.

B.8. *NGC4536*

NGC4536 is a SAB(rs)bc type galaxy located in the Virgo Cluster at a measured systemic velocity of $v_{sys} = 1867 \pm 33\ \mathrm{km\,s^{-1}}$ and inclination $i = 61°$. The data on the receding side of NGC4536 is quite messy, and may include contamination from background sources. Hence, our measured systemic velocity, and thus rotation velocity of 139 ± 37 $\mathrm{km\,s^{-1}}$, have relatively high uncertainty. Other published redshift values available from NED and rotation velocities from the HyperLEDA database are broadly consistent with our values, albeit biased slightly lower and higher in velocity, respectively.

There are 2 sightlines to the southwest of NGC4536, both on the receding side of the galaxy. HE1228+0131 at $\rho = 338$ kpc and 86° azimuth has 5 Lyα lines: $v_{\mathrm{Ly}\alpha} = 1495, 1571, 1686, 1721, 1854\ \mathrm{km\,s^{-1}}$ ($\Delta v = -372, -296, -181, -146, -13$ $\mathrm{km\,s^{-1}}$). None of these are of the correct orientation for co-rotation relative to our model predictions (cylindrical = [18, 51], NFW = [2, 32] $\mathrm{km\,s^{-1}}$), and all are more likely to be associated with other nearby galaxies, such as NGC4517A, which is slightly closer to these absorbers in impact parameter and velocity than is NGC4536. At $v_{\mathrm{Ly}\alpha} = 1686$

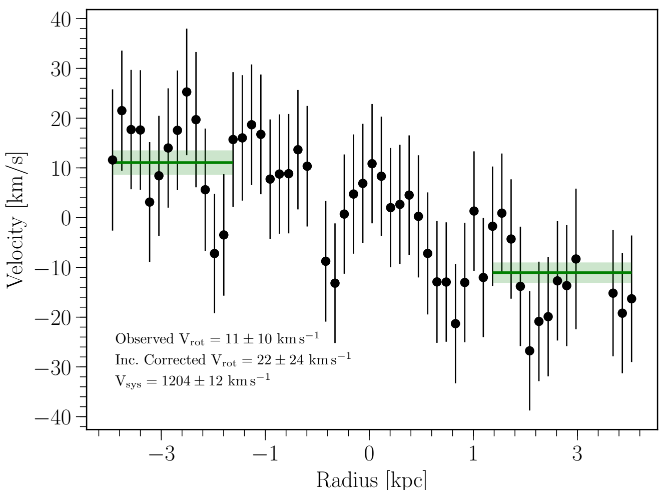

(a)

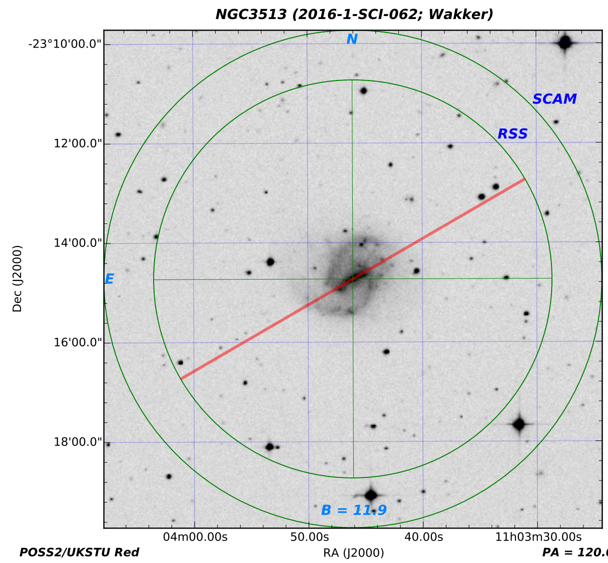

(b)

Figure 15. a) Rotation curve of NGC3513. The solid green line indicates the weighted mean velocity over the corresponding x-axis region, and the shaded green indicates the 1σ error in the mean. b) SALT finder chart for NGC3513 showing the position of the slit in red.

km s^{-1} we also detect C II, C IV, Si II, Si III, and Si IV, and at $v_{\rm Ly\alpha} = 1721$ km s^{-1} we detect Lyman series from Lyα to Lyθ as well as C II, C III, C IV, Si II, Si III, and Si IV.

The second nearby sightline is toward 3C273 at $\rho = 344$ kpc and 46° azimuth angle, and shows 3 Lyα lines at $v_{\rm Ly\alpha} = 1580, 2156, 2267$ km s^{-1} ($\Delta v = -287, 289, 400$ km s^{-1}). Two of these are correctly oriented for co-rotation relative to our model predictions (cylindrical = [87, 121], NFW = [5, 41] km s^{-1}), but are too high in velocity to make this scenario probable. Overall, given the number of nearby galaxies and their locations, we would expect these absorbers to trace the overall velocity field instead of the halo rotation of any particular galaxy.

Just remove this target entirely? Or leave this discussion in place and not include it in the statistics? In this draft I have removed it entirely from the results.

B.9. *NGC4939*

NGC4939 is a large, fast rotating ($v_{\rm rot} = 275 \pm 49$ km s^{-1}) SA(s)bc type galaxy with measured systemic velocity $v_{\rm sys} = 3093 \pm 33$ km s^{-1} and inclination $i = 48°$. The background QSO PG1302-102 is located southeast at $\rho = 254$ kpc and 61° azimuth angle on the approaching side of NGC4939. We detect a Lyα absorber at $v_{\rm Ly\alpha} = 3448$ km s^{-1} ($\Delta v = 355$km s^{-1}) towards PG1302-102. As this absorber is located on the approaching side, we can easily rule out co-rotation in this case. NGC4939 does not have any close neighbors, so represents an intriguing case against co-rotation for gas past $1R_{\rm vir}$.

B.10. *NGC5364*

NGC5364 is a SA(rs)bc pec type galaxy at a measured systemic velocity $v_{\rm sys} = 1238 \pm 17$ km s^{-1} and inclination $i = 57°$. It is located in a group environment with 5 other large, nearby galaxies. The background QSO SDSSJ135726.27+043541.4 is located southeast at $\rho = 165$ kpc and 84° azimuth angle on the receding side of NGC5364. We detect Lyα at $v_{\rm Ly\alpha} = 967, 1124$ km s^{-1} ($\Delta v = -271, -114$ km s^{-1}) toward SDSSJ135726.27+043541.4. These absorbers have the opposite sign for co-rotation relative to our model predictions (cylindrical = [-26, 108], NFW = [-30, 68] km s^{-1}). However, because of the orientation of NGC5364 on the sky with respect to this sightline, these absorbers lie extremely close to the inflection point were projected rotation velocities flip to approaching instead of receding. For example, shifting the location of SDSSJ135726.27+043541.4 east by a tenth of a degree (~ 20 kpc) is sufficient to put these absorbers on the approaching side of NGC5364. Hence, both of these absorbers could be co-rotating with NGC5364 given very reasonable assumptions on the shape of an extended disk. Nonetheless, the fact that this system lives in galaxy group environment likely dominates the surrounding velocity field.

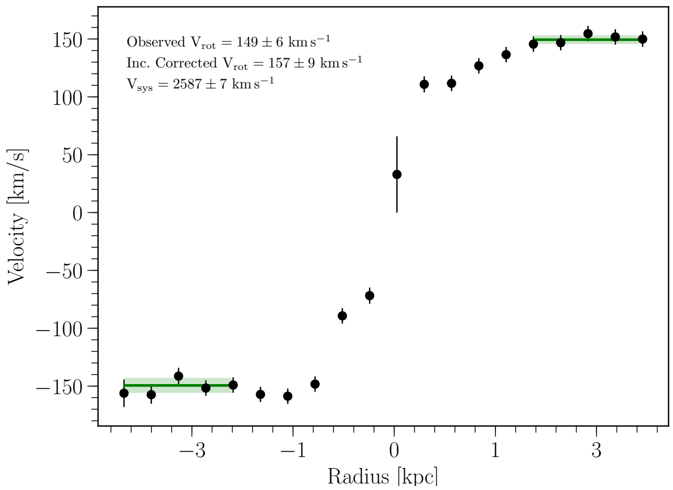

(a)

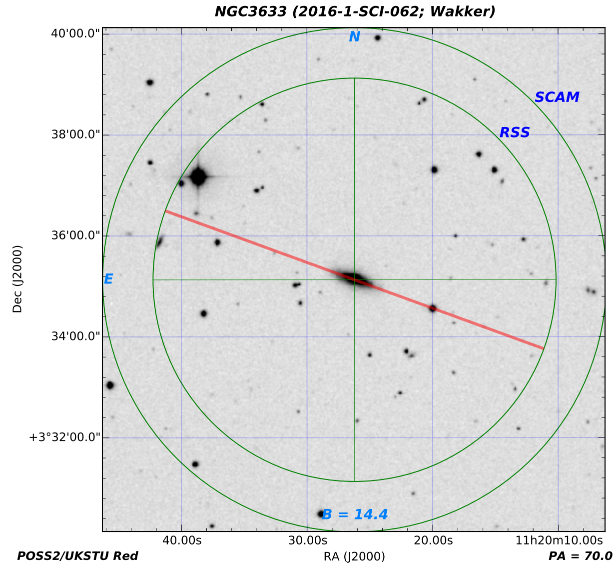

(b)

Figure 16. a) Rotation curve of NGC4536. The solid green line indicates the weighted mean velocity over the corresponding x-axis region, and the shaded green indicates the 1σ error in the mean. b) SALT finder chart for NGC3633 showing the position of the slit in red.

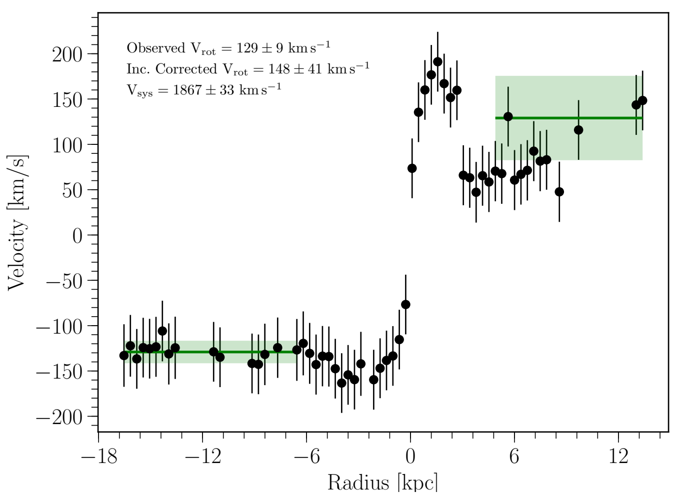

(a)

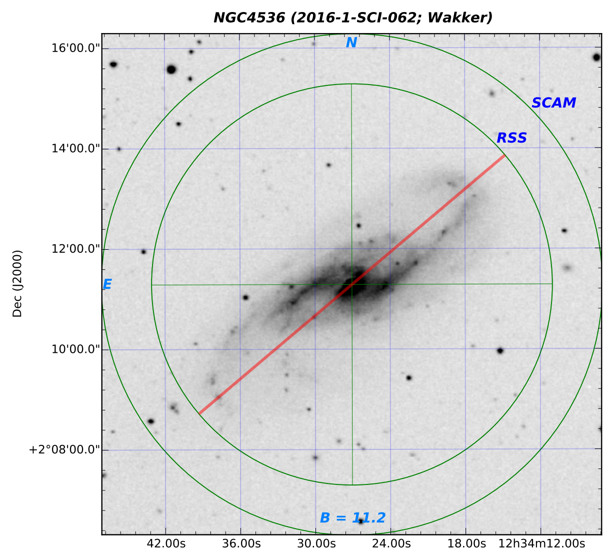

(b)

Figure 17. a) Rotation curve of NGC4536. The solid green line indicates the weighted mean velocity over the corresponding x-axis region, and the shaded green indicates the 1σ error in the mean. b) SALT finder chart for NGC4536 showing the position of the slit in red.

B.11. *NGC5786*

NGC5786 is a large, strongly-barred spiral galaxy with measured systemic velocity $v_{\rm sys} = 2975 \pm 22$ km s^{-1} and inclination $i = 65°$. The background QSO QSO1500-4140 is located directly east at $\rho = 453$ kpc and 1° azimuth angle on the receding side of NGC5786. We detect Lyα at $v_{\rm Ly\alpha} = 3138$ km s^{-1} ($\Delta v = 163$ km s^{-1}) toward QSO1500-4140, which is slightly above the model predicted velocity range (cylindrical =[106, 160], NFW = [19, 67] km s^{-1}). However, the two neighboring galaxies ESO327-G038 and ESO327-G039 are both located south of NGC5786 at $\rho = 62, 296$ kpc,

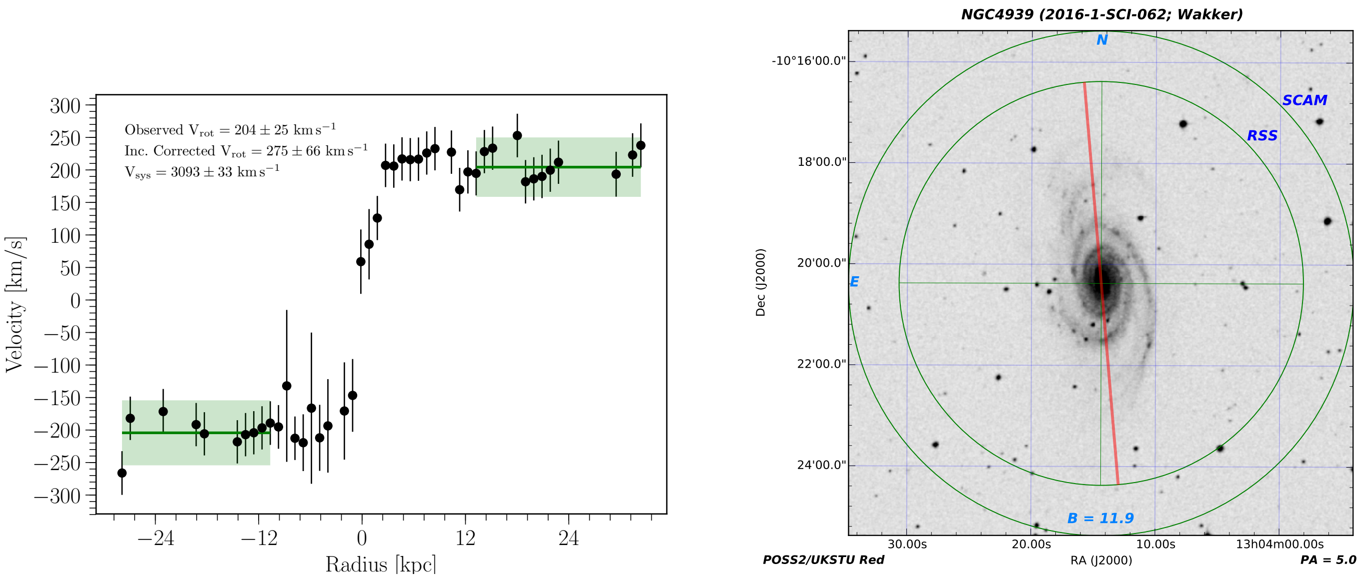

(a) (b)

Figure 18. a) Rotation curve of NGC4939. The solid green line indicates the weighted mean velocity over the corresponding x-axis region, and the shaded green indicates the 1σ error in the mean. b) SALT finder chart for NGC4939 showing the position of the slit in red.

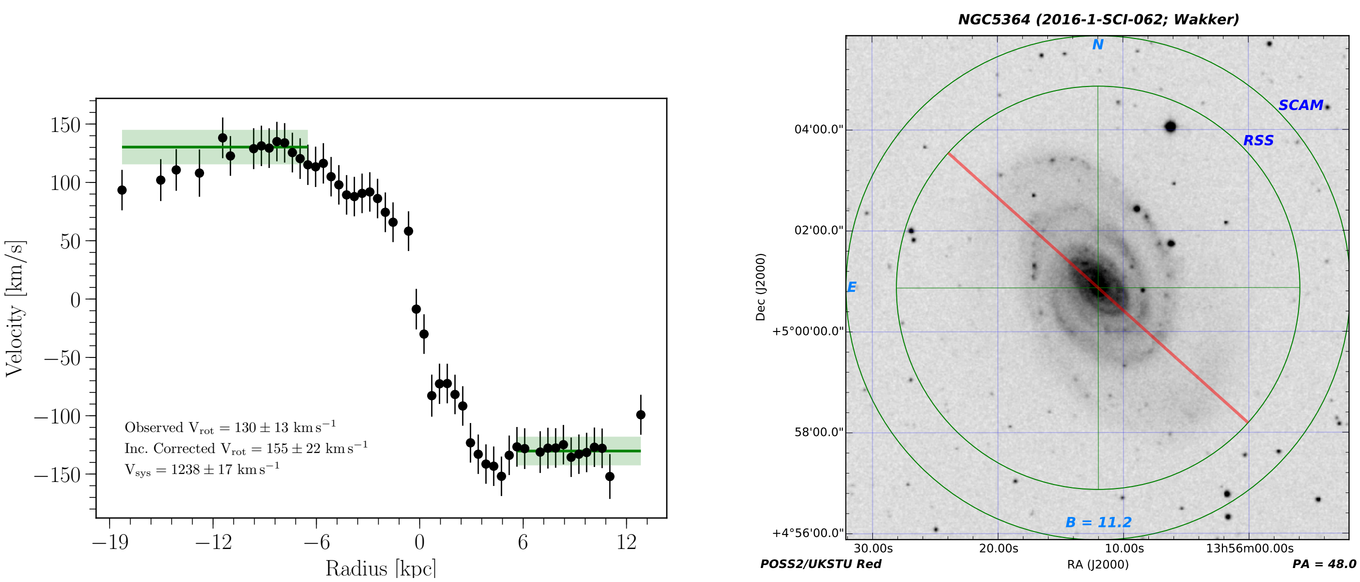

(a) (b)

Figure 19. a) Rotation curve of NGC5364. The solid green line indicates the weighted mean velocity over the corresponding x-axis region, and the shaded green indicates the 1σ error in the mean. b) SALT finder chart for NGC5364 showing the position of the slit in red.

respectively. These nearby galaxies, along with the large distance to the absorption ($\sim 2.5R_{\rm vir}$), make it difficult to believe this as evidence of an NGC5786 extended disk.

B.12. *UGC09760*

UGC09760 is an edge-on, slow-rotating Sd galaxy with measured systemic velocity $v_{\rm sys} = 2094 \pm 16$ km s^{-1}. This systemic velocity deviates slightly from other published redshifts, such as the The Updated Zwicky Catalog value of

$v_{\rm sys} = 2023 \pm 2$ km s^{-1} (Falco et al. 1999). This is likely due to our method of imposing rotation symmetry and averaging the approaching and receding velocities to derive $v_{\rm sys}$. If we do not sample the rotation curve far enough out, a systematic offset is not unreasonable. Indeed, we do not detect the rotation curve turnover or flattening point.

The background QSO SDSSJ151237.15+012846.0 is located southeast at $\rho = 123$ kpc and 90° azimuth angle. We detect Lyα absorption at $v_{\rm Ly\alpha} = 2029$ km s^{-1} ($\Delta v = -65$ km s^{-1}) toward SDSSJ151237.15+012846.0. This velocity falls outside the model predictions for co-rotation (cylindrical = [-30, 30], NFW = [-30, 86] km s^{-1}), but unfortunately this sightline lies almost exactly at an azimuth of 90°. Hence, the motion of this gas could easily be either co-rotating or counter-rotating depending on a minute change in the position angle assigned to UGC09760. This is especially true if we assume our measured v_{sys} is erroneously high, and indeed closer to the values obtained by other observations. For example, if we adjust the position angle by a single degree, to 56° instead of 57°, our model predictions become (cylindrical = [-30, 30] , NFW = [-79, 30] km s^{-1}) and this absorber becomes consistent with co-rotation in the NFW model.

It is worth noting that there are several small satellite galaxies nearby, including SDSSJ151208.16+013508.5, SDSSJ151121.63+013637.6, SDSSJ151241.38+013723.7 and UGC09746 (impact parameters $\rho = 53, 88, 82, 230$ kpc respectively). All of these galaxies lie slightly blue-ward of UGC09760, and thus *farther* away in velocity from the Lyα absorber at 2029 km s^{-1}.

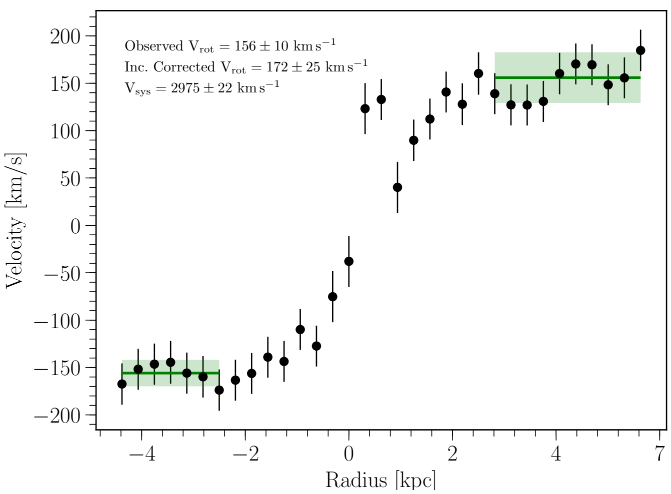

(a)

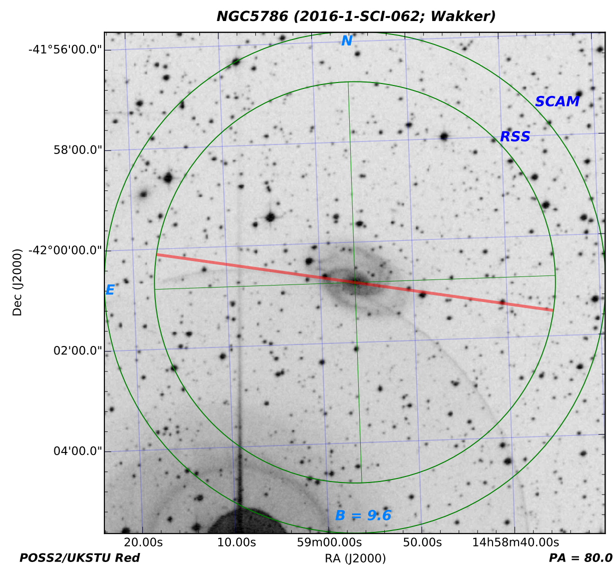

(b)

Figure 20. a) Rotation curve of NGC5786. The solid green line indicates the weighted mean velocity over the corresponding x-axis region, and the shaded green indicates the 1σ error in the mean. b) SALT finder chart for NGC5786 showing the position of the slit in red.

C. ANCILLARY DATA

To increase our sample size we have also searched the literature for galaxies with published rotation curves and orientations. Unfortunately, while the rotation velocity is available for thousands of galaxies, only a handful also include the *orientation* of the rotation on the sky. Of these, we were able to find 18 additional galaxies which have a systemic velocity greater than ~ 500 km s^{-1}, and are near to a COS or STIS sightline with available data. We have included the 5 galaxy-QSO systems analyzed by Côté et al. (2005). We briefly summarize each of these systems here (see Sections C.9 - ????), and refer the reader to Côté et al. (2005) for a more complete discussion. As new spectra and redshift-independent distances are available for these systems our results, while similar, are not identical.

C.1. *NGC3198*

NGC3198 is a SB(rs)c type galaxy with systemic velocity $v_{\rm sys} = 661 \pm 3$ km s^{-1}and inclination = $i = 70°$. It is a well studied galaxy, and is included the detailed THINGS rotation curve study of de Blok et al. (2008). We extracted the raw

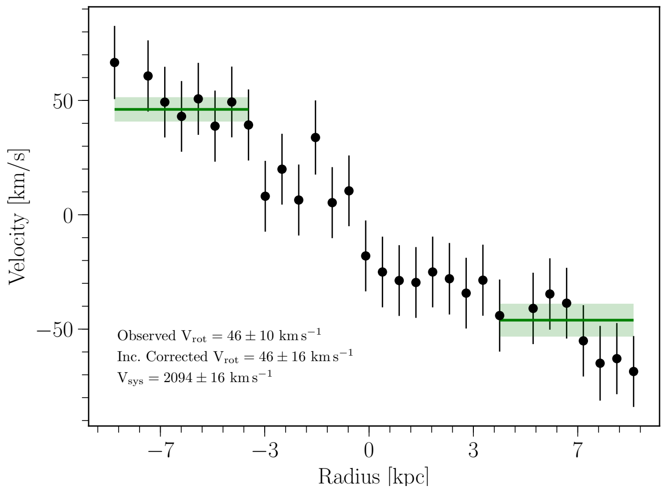

(a)

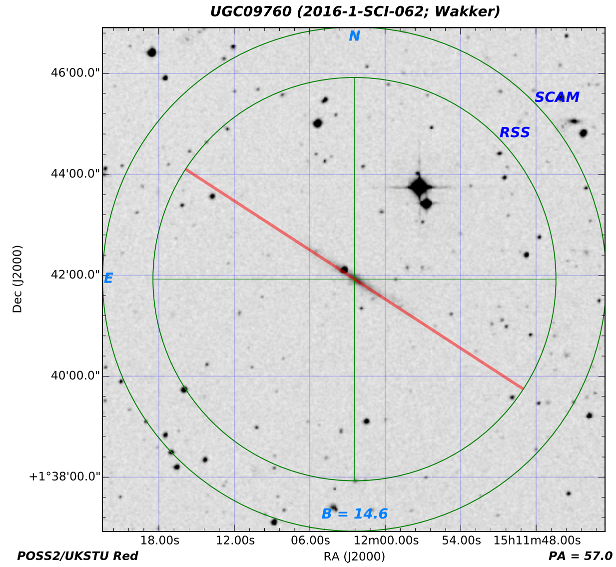

(b)

Figure 21. a) Rotation curve of UGC09760. The solid green line indicates the weighted mean velocity over the corresponding x-axis region, and the shaded green indicates the 1σ error in the mean. b) SALT finder chart for UGC09760 showing the position of the slit in red.

rotation curve derived by de Blok et al. (2008) using the plot digitization software WebPlotDigitizer[3]. NGC3198 has an even and flat rotation curve, with an average velocity of $v_{\rm rot} = 152$ km s^{-1}. The background QSO RX_1017.5+4702 is located northeast at $\rho = 370$ kpc and 55° azimuth angle on the approaching side of NGC3198. We detect Lyα toward RX_1017.5+4702 at $v_{\rm Ly\alpha} = 629$ km s^{-1} ($\Delta v = -32$ km s^{-1}), which can nicely be described by a co-rotating disk based on our model predicted velocity range (cylindrical = [-153, -21], NFW = [-91, 6] km s^{-1}). We note that the small dwarf galaxy SDSSJ101848.77+452137.0 is located 65 kpc away from NGC3198 toward the southwest.

C.2. *NGC3351*

NGC3351 is a mostly face-on ($i = 29°$) SB(r)b type galaxy with systemic velocity $v_{\rm sys} = 778 \pm 4$ km s^{-1}. It is located ~ 200 kpc southwest of the core of the Leo I group. We take the rotation curve and orientation produced by Dicaire et al. (2008). While we expect any extended disk rotation to be quickly disrupted due to the complex Leo I environment, this galaxy also has one of the closest sightlines in our sample with SDSSJ104335.90+115129.0 at $\rho = 31$ kpc and 13° azimuth on the northwest, approaching side. We detect Lyα at $v_{\rm Ly\alpha} = 717, 882, 1030$ km s^{-1}($\Delta v = -61, 104, 252$ km s^{-1}) toward this sightline. The lowest velocity absorber agrees nicely with both models for co-rotation, while the other two are above our model predictions (cylindrical = [-99, 12], NFW = [-68, 20] km s^{-1}). We also detect multiple metal ions associated with $v_{\rm Ly\alpha} = 717$ km s^{-1} line, including C II, N I, N V, O I, Si II, Si III, Si IV, S II, and Fe II.

C.3. *NGC5907*

NGC5907 is a large, edge-on SA(s)c type galaxy with systemic velocity $v_{\rm sys} = 670 \pm 3$ km s^{-1}. We take the rotation curve and orientation produced by Yim et al. (2014). The background QSO SBS1503+570 is located northwest at $\rho = 413$ kpc and 47° azimuth angle on the receding side of NGC5907. We detect Lyα at $v_{\rm Ly\alpha} = 708$ km s^{-1} ($\Delta v = 38$ km s^{-1}), which falls within the model predictions for co-rotation (cylindrical = [31, 228], NFW = [-24, 101] km s^{-1}). Unfortunately there are several other nearby galaxies, the largest of which being NGC5866 (diameter $D = 20.8$ and impact parameter $\rho = 208$ kpc, versus for NGC5907 - $D = 50.6$ and $\rho = 413$ kpc). Hence, it is difficult to assign this absorber to NGC5907 alone.

C.4. *NGC4565*

NGC4565 is an edge-on SA(s)b type galaxy with systemic velocity $v_{\rm sys} = 1230 \pm 5$ km s^{-1}. We take the rotation curve and orientation produced by Sofue (1996). The background QSO RX_J1236.0+2641 is located directly north at

[3] WebPlotDigitizer; http://arohatgi.info/WebPlotDigitizer

$\rho = 147$ kpc and 41° azimuth angle on receding side of NGC4565. We detect Lyα absorption at $v_{\mathrm{Ly}\alpha} = 1009, 1166, 1254$ km s^{-1} ($\Delta v = -221, -64, 24$ km s^{-1}) toward RX_J1236.0+2641. Only the $v_{\mathrm{Ly}\alpha} = 1254$ km s^{-1} line is consistent with co-rotating gas relative to our model predictions (cylindrical = [-2, 246], NFW = [-30, 144] km s^{-1}). However, the presence of several other nearby galaxies (e.g., NGC4559, NGC4562) surely disrupts any possible extended disk rotation that would otherwise be detectable via sightline absorption.

C.5. *UGC06446*

UGC06446 is a Sd type galaxy with systemic velocity $v_{\mathrm{sys}} = 644 \pm 1$ km s^{-1} and inclination $i = 48°$ on the far northwest edge of the Ursa Major cluster of galaxies. We take the rotation curve and orientation information produced by (Verheijen & Sancisi 2001; Swaters et al. 2009). The background QSO SDSSJ112448.30+531818.0 is located southwest at $\rho = 143$ kpc and 22° azimuth angle on the receding side of UGC06446. We detect Lyα at $v_{\mathrm{Ly}\alpha} = 664, 1019$ km s^{-1} ($\Delta v = 20, 375$ km s^{-1}). The absorber at $v_{\mathrm{Ly}\alpha} = 664$ falls well within our model predicted co-rotation range (cylindrical = [-9, 65], NFW = [-15, 61] km s^{-1}), but the absorber at $v_{\mathrm{Ly}\alpha} = 1019$ is far more likely to be associated with NGC3631 ($\rho = 86$ kpc, $v_{\mathrm{sys}} = 1156$ km s^{-1}). We therefore treat these as separate systems.

C.6. *NGC3631*

NGC3631 is a mostly face-on ($i = 17°$) SA(s)c type galaxy with systemic velocity $v_{\mathrm{sys}} = 1156 \pm 1$ km s^{-1}. We take the rotation curve and orientation information produced by Knapen (1997). There are 4 nearby QSOs, which we will present in order of increasing impact parameter.

First, the closest background QSO RX_J1117.6+5301 is located southwest at $\rho = 78$ kpc and 75° azimuth angle on the receding side of NGC3631. We detect Lyα at $v_{\mathrm{Ly}\alpha} = 1131, 1259$ km s^{-1} ($\Delta v = -25, 103$ km s^{-1}). Both of these lines fall outside of our model predicted velocities (cylindrical = [10, 24], NFW = [1, 21] km s^{-1}).

Second, background QSO SDSSJ112448.30+531818.0 is located northeast at $\rho = 86$ kpc and 74° azimuth angle on the approaching side of NGC3631. We detect Lyα at $v_{\mathrm{Ly}\alpha} = 1019, 1141$ km s^{-1} ($\Delta v = -137, -15$ km s^{-1}). Only the higher velocity absorber falls within our model predicted velocity range (cylindrical = [-26, -11], NFW = [-22, 1] km s^{-1}).

Third, the background QSO SDSSJ111443.70+525834.0 is located in the same direction but farther than RX_J1117.6+5301, at $\rho = 145$ kpc and 72° azimuth angle on the receding side of NGC3631. We detect Lyα at $v_{\mathrm{Ly}\alpha} = 1163$ km s^{-1} ($\Delta v = 7$ km s^{-1}). This absorber appears to agree well with our model predicted velocity range (cylindrical = [8, 29], NFW = [-5, 24] km s^{-1}).

Finally, the background QSO SBS1116+523 is located south at $\rho = 163$ kpc and 40° azimuth angle on the approaching side of NGC3631, but we do not detect any Lyα within ± 400 of NGC3631.

Unfortunately, while this galaxy has 4 nearby QSOs, there are also numerous other large galaxies that are likely disturbing any extended velocity field from NGC3631. The closest of these are NGC3657 ($\rho = 75$ kpc, $D = 6.3$ kpc, $v_{\mathrm{sys}} = 1215$ km s^{-1}), and UGC06251 ($\rho = 181$ kpc, $D = 10.2$ kpc, $v_{\mathrm{sys}} = 1146$ km s^{-1}).

C.7. *NGC3726*

NGC3726 is a SAB(r)c type galaxy with systemic velocity $v_{\mathrm{sys}} = 866 \pm 1$ km s^{-1} and inclination $i = 52°$ on the southwestern edge of the Usra Major galaxy cluster (Verheijen & Sancisi 2001). The closest background QSO, CSO1208, is located southeast at $\rho = 369$ kpc and 88° azimuth angle on the receding side of NGC3726. We detect Lyα at $v_{\mathrm{Ly}\alpha} = 731, 874$ km s^{-1} ($\Delta v = -135, 8$ km s^{-1}) toward CSO1208. Only the higher velocity absorber falls within our predicted velocity range (cylindrical = [-27, 29], NFW = [-28, 21] km s^{-1}). A more distant QSO, RX_J1142.7+4625, is located in the same direction as CSO1208 at $\rho = 440$ kpc and 86° azimuth angle on the approaching side of NGC3726. We detect Lyα at $v_{\mathrm{Ly}\alpha} = 818$ km s^{-1} ($\Delta v = -48$ km s^{-1}), which falls just outside our predicted velocity range (cylindrical = [-34, -14], NFW = [-30, -7] km s^{-1}).

These two QSOs lie very close to and on apposing sides of the minor axis, such that CSO1208 samples the receding side and RX_J1142.7+4625 the approaching. Unfortunately, both are also closer to a small group of dwarf galaxies, including NGC3782 and MCG+08-21-092, ~ 100 km s^{-1} blueward of NGC3726. The $v_{\mathrm{sys}} = 731$ km s^{-1} line toward CSO1208 is likely associated with this dwarf group, and the other lines may also be.

C.8. *NGC3067*

NGC3067 is a mostly edge-on ($i = 68°$) SAB(s)ab type galaxy with systemic velocity $v_{\mathrm{sys}} = 1465 \pm 5$ km s^{-1}. This galaxy and the nearby QSO sightline toward 3C232 is a particularly well studied system. They are separated by only $\rho = 11$ kpc (74° azimuth angle on the northwest, receding side) and a Lyman Limit System (LLS) with column density $N_{HI} = 1 \times 10^{20}$ cm^{-2} is detected toward 3C232 at $v_{\mathrm{Ly}\alpha} = 1408$ km s^{-1}, which has been postulated as a high velocity cloud (HVC) orbiting NGC3067 (Carilli et al. 1989; Keeney et al. 2005).

We obtained the rotation curve for NGC3067 from Rubin et al. (1982) and the orientation from Carilli et al. (1989). While H I measurements of this LLS fit a single component (at $v_{\rm H\,I} = 1421$ km s^{-1}), we have fit 3 separate components at $v_{\rm Ly\alpha} = 1408, 1510, 1641$ km s^{-1} ($\Delta v = -57, 45, 176$ km s^{-1}) to match the associated metal lines (namely, C IV, Si II, Si III, Si IV, Mg II, Fe II, and N I all show at least 2 separate components). This splitting has been analyzed in detail most recently by Keeney et al. (2005) and Stocke et al. (2010), who find similar but slightly lower $v_{\rm Ly\alpha}$ for all three absorbers. Only the lowest velocity component is can strictly be described by our model velocity range (cylindrical = [-121, 25], NFW = [-139, 26] km s^{-1}), however the $v_{\rm Ly\alpha} = 1510$ km s^{-1} component is also very close to this range. The $v_{\rm Ly\alpha} = 1641$ km s^{-1} component, however, must be either a counter-rotating cloudlet or an outflow directed away from our line of sight.

A second QSO SDSSJ095914.80+320357.0 is located farther away, to the southeast at $\rho = 128$ kpc and 43° azimuth angle on the receding side of NGC3067. We detect Lyα at v$_{\rm Ly\alpha} = 1493$ km s^{-1} ($\Delta v = 28$ km s^{-1}), which agrees well with our model predicted velocity range (cylindrical = [11, 138], NFW = [-12, 81] km s^{-1}).

C.9. *NGC6140*

NGC6140 is a small SB(s)cd type galaxy with systemic velocity $v_{\rm sys} = 910 \pm 4$ km s^{-1} and inclination $i = 45°$. We take the rotation curve and orientation information produced by Côté et al. (2005). A background QSO MRK876 is located northwest at $\rho = 113$ kpc and azimuth angle 21° (although this is somewhat uncertain; the position angle for NGC6140 could be closer to 60° than our adopted value of 94° due to it being mostly face on, faint, and strongly barred). We detect Lyα at $v_{\rm Ly\alpha} = 939$ km s^{-1} ($\Delta v = 29$ km s^{-1}) toward MRK876. This absorber velocity is of the correct *sign*, but just under the the model predicted velocity range (cylindrical = [40, 101], NFW = [35, 102] km s^{-1}) for co-rotation. However, this absorber is still likely co-rotating given both the velocity and position angle uncertainties. Additionally, we detect Lyβ and O VI associated with this Lyα absorber.

C.10. *NGC4529*

NGC4529 is an edge-on and isolated Scd type galaxy with systemic velocity $v_{\rm sys} = 2536 \pm 11$ km s^{-1}. We take the rotation curve and orientation information produced by Côté et al. (2005). The QSO MRK771 is located west at $\rho = 159$ kpc and 23° azimuth angle on the approaching side of NGC4529. We detect Lyα at $v_{\rm sys} = 2553$ km s^{-1} ($\Delta v = 17$ km s^{-1}), which is anti-rotating relative to our model predictions (cylindrical = [-103, -40], NFW = [-87, -25] km s^{-1}). As Côté et al. (2005) conclude, "there is simply no physical way to produce such a velocity with an extending co-rotating disk."

C.11. *UGC04238*

UGC04238 is an isolated and edge-on SBd type galaxy with systemic velocity $v_{\rm sys} = 1544 \pm 7$ km s^{-1}. We take the rotation curve and orientation information produced by Côté et al. (2005). The background QSO PG0804+761 is located directly south at $\rho = 148$ kpc and 59° azimuth on the receding side of UGC04238. We detect Lyα at $v_{\rm Ly\alpha} = 1526, 1593$ km s^{-1} ($\Delta v = -18, 49$ km s^{-1}) toward PG0804+761. Relative to our model predictions (cylindrical = [-3, 86], NFW = [-10, 75] km s^{-1}), although both are close, only the absorber at 1593 km s^{-1} (the lower EW of the two) falls within the expected velocity range for co-rotation.

C.12. *NGC2770*

NGC2770 is a large, edge-on Sc type galaxy with systemic velocity $v_{\rm sys} = 1948 \pm 2$ km s^{-1}. It is mostly isolated except for two nearby small dwarfs MCG+06-20-036NED02 and GALEXASCJ090946.88+330840.4 (both 25 kpc away, on opposite sides of NGC2770). We take the rotation curve and orientation information produced by Rhee & van Albada (1996). There are five nearby QSOs, which we present in order of increasing impact parameter.

First, the QSO FBQSJ0908+3246 is located south at $\rho = 204$ kpc and 59° azimuth angle on the approaching side of NGC2770. We detect Lyα at $v_{\rm Ly\alpha} = 1915, 1982$ km s^{-1} ($\Delta v = -33, 34$ km s^{-1}). Relative to our model predictions (cylindrical = [-146, -4], NFW = [-117, 10] km s^{-1}), only the lower velocity line can be described as co-rotating.

Second, the QSO TON1015 is located northeast at $\rho = 218$ kpc and 61° azimuth angle on the receding side of NGC2770. We detect Lyα at $v_{\rm Ly\alpha} = 1833, 1985$ km s^{-1} ($\Delta v = -115, 37$ km s^{-1}). Relative to our model predictions (cylindrical = [3, 146], NFW = [-10, 115] km s^{-1}), only the higher velocity absorber can be described as co-rotating.

Third the QSO SDSSJ091127.30+325337.0 is located southeast at $\rho = 234$ kpc and 30° azimuth angle on the approaching side of NGC2770. We detect Lyα at $v_{\rm Ly\alpha} = 2063$ km s^{-1} ($\Delta v = 115$ km s^{-1}). Relative to our model predictions (cylindrical = [-150, -43], NFW = [-117, -19] km s^{-1}), this absorber appears to be counter-rotating.

Fourth, the QSO SDSSJ091052.80+333008.0 at is located northeast at $\rho = 239$ kpc and 66° azimuth angle on the receding side of NGC2770. We detect Lyα at $v_{\rm sys} = 1824, 1975$ km s^{-1} ($\Delta v = -124, 27$ km s^{-1}). Relative to our model predictions (cylindrical = [6, 145], NFW = [-7, 112] $\mathrm{km\,s^{-1}}$), only the higher velocity absorber can be described as co-rotating.

Finally, the QSO TON1009 is located south at $\rho = 267$ kpc and 41° azimuth angle on the approaching side of NGC2770. We detect Lyα at $v_{\mathrm{sys}} = 1908, 1980$ $\mathrm{km\,s^{-1}}$ ($\Delta v = -40, 32$ $\mathrm{km\,s^{-1}}$). Relative to our model predictions (cylindrical = [-146, -39], NFW = [-110, -14] $\mathrm{km\,s^{-1}}$), only the lower velocity absorber can be described as co-rotating.

Interestingly, we appear to be detecting extended gas structures in these 5 sightlines. Toward the northeast we find TON1015 and SDSSJ091052.80+333008.0 and a set of absorber pairs at $v_{\mathrm{Ly}\alpha} = 1833, 1824$ $\mathrm{km\,s^{-1}}$ and $v_{\mathrm{Ly}\alpha} = 1985, 1975$ $\mathrm{km\,s^{-1}}$ each having very similar EW and $N_{\mathrm{H\,I}}$, and remarkably similar appearing line-structure. Adopting a distance of 28.6 Mpc to this cloud, we calculate a linear separation between TON1015 and SDSSJ091052.80+333008.0 of 28 kpc. Hence, there appears to be two distinct clouds of at least 28 kpc in physical extent sandwiched around the system velocity of NGC2770. Toward the south we find TON1009 and FBQSJ0908+3246 and a set of absorber pairs at $v_{\mathrm{Ly}\alpha} = 1908, 1915$ $\mathrm{km\,s^{-1}}$ and $v_{\mathrm{Ly}\alpha} = 1980, 1982$ $\mathrm{km\,s^{-1}}$, again with similar EW, $N_{\mathrm{H\,I}}$ and line-shapes. **SHOULD I ELABORATE? COMPARE TO MILKY WAY - MAGELLANIC SYSTEM?**

C.13. *NGC3432*

NGC3432 is an edge-on SB(s)m type galaxy with systemic velocity $v_{\mathrm{sys}} = 616 \pm 4$ $\mathrm{km\,s^{-1}}$. It is interacting with the nearby dwarf galaxy UGC05983 located 11 kpc away and at $v_{\mathrm{sys}} = 765$ $\mathrm{km\,s^{-1}}$. We take a rotation curve and orientation for NGC3432 from Rhee & van Albada (1996). The QSO CSO295 is located just 20 kpc away and just to the receding side of the minor axis (82° azimuth angle). This is the second closest pair in our sample, after the 11 kpc separated NGC3067-3C232 system. We detect Lyα at $v_{\mathrm{Ly}\alpha} = 600, 662$ $\mathrm{km\,s^{-1}}$ ($\Delta v = -16, 46$ $\mathrm{km\,s^{-1}}$) toward CSO295. Relative to our model predictions (cylindrical = [-37, 48], NFW = [-37, 134] $\mathrm{km\,s^{-1}}$) both of these absorbers are consistent with co-rotation. In fact, this orientation would represent the lower-velocity cloud existing toward the near-edge of the halo and the higher velocity cloud lying very close to the plane of the stellar disk. We also detect C II, Si II, Si III, and Si IV associated with this absorption system.

A second QSO RX_J1054.2+3511 is located south at $\rho = 290$ kpc and 57° azimuth angle on the receding side of NGC3432. We detect Lyα at $v_{\mathrm{sys}} = 703$ $\mathrm{km\,s^{-1}}$ ($\Delta v = 87$ $\mathrm{km\,s^{-1}}$) toward RX_J1054.2+3511. Relative to our model predictions (cylindrical = [0, 123], NFW = [-9, 111] $\mathrm{km\,s^{-1}}$), this absorber is consistent with co-rotation as well.

Bart - SDSSJ105231.02+363709.6, SDSSJ105229.19+363649.8, SDSSJ105233.13+363736.7, SDSSJ105240.79+363953.7 are all actually part of NGC3432. I've discovered a few cases of this in the galaxy table, but have not had any time to address it.

C.14. *NGC3666*

NGC3666 is a mostly isolated and edge-on SA(rs)c type galaxy with systemic velocity $v_{\mathrm{sys}} = 1060 \pm 1$ $\mathrm{km\,s^{-1}}$. We take the rotation curve and orientation information produced by Rhee & van Albada (1996). The QSO SDSSJ112439.50+113117.0 is located north at $\rho = 58$ kpc and 83° azimuth angle on the approaching side of NGC3666. We detect Lyα at $v_{\mathrm{sys}} = 1047, 1099$ $\mathrm{km\,s^{-1}}$ ($\Delta v = -13, 39$ $\mathrm{km\,s^{-1}}$) toward SDSSJ112439.50+113117.0. Relative to our model predictions (cylindrical = [-87, 20], NFW = [-136, 20] $\mathrm{km\,s^{-1}}$) the lower velocity absorber is consistent with co-rotation, while the other is slightly too high in velocity.

C.15. *NGC5951*

NGC5951 is a large, edge-on SBc type galaxy with systemic velocity $v_{\mathrm{sys}} = 1780 \pm 1$ $\mathrm{km\,s^{-1}}$. We take the rotation curve and orientation for NGC5951 from Rhee & van Albada (1996). The QSO 2E1530+1511 is located east at $\rho = 55$ kpc and 85° azimuth angle on the receding side of NGC5951. We detect Lyα at $v_{\mathrm{Ly}\alpha} = 1795, 1953$ $\mathrm{km\,s^{-1}}$ ($\Delta v = 15, 173$ $\mathrm{km\,s^{-1}}$) toward 2E1530+1511. Relative to our model predictions (cylindrical = [-31, 114], NFW = [-32, 125] $\mathrm{km\,s^{-1}}$), the lower velocity absorber is consistent with co-rotation while the other is a bit outside of the upper range. The pair of galaxies NGC5954 and NGC5953 are nearby (~ 100 kpc), but the sightline toward 2E1530+1511 is closer and on the opposite side of NGC5951. Given the systemic velocity for the nearby galaxies NGC5954 and NGC5953 ($v_{\mathrm{sys}} = 1959, 1965$ $\mathrm{km\,s^{-1}}$), this absorber is likely also linked with that system.

C.16. *NGC7817*

NGC7817 is an edge-on SAbc type galaxy with systemic velocity $v_{\mathrm{sys}} = 2309 \pm 4$ $\mathrm{km\,s^{-1}}$. We take the rotation curve and orientation information produced by Rhee & van Albada (1996). The background QSO MRK335 is located southeast at $\rho = 343$ kpc and almost directly along the minor axis of NGC7817 (90° azimuth angle). We detect Lyα at $v_{\mathrm{sys}} = 1954, 2274$ $\mathrm{km\,s^{-1}}$ ($\Delta v = -355, -35$ $\mathrm{km\,s^{-1}}$) toward MRK335. Because these absorbers lie almost exactly along the minor axis, our model predicts a very narrow velocity range for co-rotation (cylindrical = [-26, -24], NFW

= [-26, -24] $\mathrm{km\,s^{-1}}$). While the higher velocity line falls a mere 9 $\mathrm{km\,s^{-1}}$ outside this predicted range, the absorption at 1954 $\mathrm{km\,s^{-1}}$ is likely not directly associated with NGC7817 given the large velocity difference. Additionally, the neighboring dwarf galaxy ESDOF538-02 ($v_{\rm sys}$ = 2175 $\mathrm{km\,s^{-1}}$) appears in the same direction as MRK335 and only $\rho = 57$ kpc away from NGC7817, and NSA126180 ($v_{\rm sys}$ = 1950 $\mathrm{km\,s^{-1}}$) appears only $\rho = 83$ kpc away from MRK335.

C.17. *UGC08146*

UGC08146 is an isolated and edge-on Sd type galaxy with systemic velocity $v_{\rm sys} = 670 \pm 1$ $\mathrm{km\,s^{-1}}$. This galaxy (and the nearby QSO PG1259+593) are included in the Côté et al. (2005) sample also, but we have taken the rotation curve and orientation information from Rhee & van Albada (1996). The QSO PG1259+593 is located northwest at $\rho = 114$ kpc at 50° azimuth angle on the receding side of UGC08146. While Côté et al. (2005) cite a single Lyα component at $v_{\rm Ly\alpha}$ = 679 $\mathrm{km\,s^{-1}}$, we detect two components at $v_{\rm Ly\alpha} = 646, 683$ $\mathrm{km\,s^{-1}}$ ($\Delta v = -24, 13$ $\mathrm{km\,s^{-1}}$), in the higher signal-to-noise COS data now available for PG1259+593. Relative to our model predictions (cylindrical = [-13, 82], NFW = [-16, 83] $\mathrm{km\,s^{-1}}$), the higher velocity component is consistent with co-rotation, and the other component is only 8 $\mathrm{km\,s^{-1}}$ shy of falling into the NFW co-rotation range as well.

Bart - I don't think SDSSJ130206.46+584142.9 is real. Every image of it I can find is actually an image of UGC08146, so this is probably an SDSS artifact. Also, you had a note saying L=0.00 and $\rho/R_{vir} = 3.2$*? That's not true. UGC08146 diameter = 6 kpc, which is probably an underestimate, thus* $R_{vir} = 59.8$. $\rho/R_{vir} = 114/59.8 = 1.9$.